Arabian Journal of Geosciences (2023) 16:532
https://doi.org/10.1007/s12517-023-11637-1

ORIGINAL PAPER

Petrogenesis of Late Cretaceous A_1-type alkali monogenetic volcanoes, Wadi Natash, South Eastern Desert, Egypt, and their implications for Nb mineralization and tectonic evolution

Ezz El Din Abdel Hakim Khalaf[1] · Takashi Sano[2]

Received: 12 May 2023 / Accepted: 4 August 2023 / Published online: 29 August 2023

Abstract

This article carried out an integrated study of the mineral composition, whole-rock elemental geochemistry, and zircon U-Pb dating for the rift-related alkaline volcanoes at Wadi Natash, South Eastern Desert (SED), Egypt, to investigate their magmatic evolution and origin. The Natash volcanoes (NV) are characterized by explosive and extrusive polyphases trending in NW-SE with a diverse compositional range of basalts, trachyandesites, trachytes, and rhyolites/comendites categorized by distinct high concentration of HFSEs and REEs. Zircon U-Pb dating offers ages of 96 ± 2.5 to 86 ± 2 Ma, constraining Late Cretaceous eruption of the NV. The basalts have high HFSE, REE, and Nb/U ratios similar to Nb-rich basalts derived from OIB source. The trachyandesites/trachytes and rhyolites have high ratios of Ga/Al (8–12), HFSF (Nb = 79–283 ppm, Zr = 433–1807 ppm), and REE (671–728 ppm) and low concentrations of Sr, P, Ti, and Eu which are analogous to typical A_1-type granites. The Nb enrichment in all rock types (81–283 ppm) is controlled by both magmatic and hydrothermal processes. The NV were originated from an enriched lithospheric mantle source metasomatized by asthenosphere-derived fluids and then experienced fractional crystallization (FC) with no significant input of crustal contamination. Petrographical and geochemical criteria elucidate olivine + clinopyroxene as the main fractionated phases, followed by hornblende + plagioclase + Fe-Ti oxides + apatite during the more evolved stage. In addition to FC, the phenocryst textures conform a variety of magmatic processes, such as multi-crustal storage, crystallization, volatile fluxing, and degassing and magmatic evolution in open systems with a fluctuating temperature, pressure, and water. The geothermobarometic data point to a polybaric-polythermal system with numerous magma residence regions fluctuating from lower-middle (1.4–1.25 GPa and 1154–1136 °C) to shallow crustal levels as demonstrated by plagioclase crystallization (0.75–0.26 GPa and 1048–980 °C) and Fe-Ti oxides (937–904 °C) when magmas ascend to the surface. The evolution of the NV can be linked to mantle plume magmatism and extensive Mesozoic alkaline ring complexes recorded along the Egypt/Sudan border, Northeast Africa, and Northern Arabia in an extensional setting, highlighting that the assembly of the Rodinia supercontinent might have been finalized prior to ca. 86 Ma.

Keywords A_1-type alkaline volcanoes · Nb enrichment · Magma mushes · Intracontinental extension · Alkaline ring complex

Responsible Editor: Domenico M. Doronzo

✉ Ezz El Din Abdel Hakim Khalaf
EzzKhalaf2020@gmail.com; Ezz@sci.cu.edu.eg

Takashi Sano
sano@kahaku.go.jp

[1] Geology Department, Faculty of Science, Cairo University, Giza, Egypt

[2] Department of Geology and Paleontology, National Museum of Nature and Science, Tsukuba, Japan

Introduction

Alkaline volcanoes are well-known on Earth's surface and signify low-volume monogenetic magmatism released in a single continuous explosion or in numerous intermittent rhythms in a short time (Németh, 2010). Even though the volume of the alkaline rocks is negligible, they occur broadly in anorogenic, post-collisional, and oceanic island regimes (Zhu et al., 2020; Wang et al. 2021). The rock types of alkaline volcanoes involve multicycles of basaltic, trachytic/phonolitic, and rhyolitic lava flows together with related

pyroclastic deposits, forming diverse landforms like scoria cones, tuff rings, and maar volcanoes (Brenna et al., 2012). The intrusive rocks (e.g. gabbros, syenites, and granites) are sporadically concomitant with the alkaline volcanoes. The alkaline rocks have achieved consciousness scientific and marketable attentiveness worldwide, due to its tendency to enhance total alkali, ratios of both Fe/Mg and Ga/Al, HFSEs (chiefly Nb, Ta, Zr, U), REEs, Sn, and W which characterize A-type granites (Whalen et al., 1987; Eby, 1990; Sheard et al., 2012). Although rare metal mineralizations (e.g. Nb deposits) characterizing alkaline felsic rocks have been broadly examined (Girei et al., 2019), their genesis and advancement remain a theme of controversy. Numerous theories involving a metasomatized lithospheric mantle (Zhu et al. 2016; Girei et al. 2019), lower crustal sources (Harris et al. 2018), and intricate mantle-crust itineraries (Eby 1992) have been proposed for the origin of the parental alkaline magmas.

Radical technology and equipment manufactures broadly use Nb as a vital metal (Weng et al., 2015). On Earth, large quantities of Nb mineralizations are recorded in plutonic rocks like syenites, granites, or carbonatites (Li et al., 2019). On the other hand, a scarce of Nb mineralizations is recognized in extrusive rocks, e.g. the HFSE-REE deposits in the Brockmans, Australia (Chandler and Spandler, 2020), Canada (Miller, 2015), and the Tudiling, China (Yan et al., 2022). However, these deposits are categorized by composite mineralogy with the pouring universal request for rare metals and the development of metallurgical procedures; they have fascinated ample courtesy in recent years due to their abundant assets (Chandler and Spandler 2020; Wang et al. 2021). In the previous studies, mechanisms of Nb deposits that highlight the significance of wide-ranging magmatic differentiation recognized the incompatible behaviour of these elements in rock-forming minerals (Stepanov et al., 2014), while others emphasized the role of hydrothermal alteration in organizing and enhancing rare metals (Ballouard et al., 2016). The Nb mineralization which is either formed by protracted magmatic differentiation or by hydrothermal alteration or by a mixture of both is a key point of argument (e.g. Huang et al., 2014). The role of the magmatic fractionation or hydrothermal alteration or both to increase these incompatible elements to economic ranks, raise rare metal concentrations in natural magmatic systems, and shares in the mineralizations is continually problematic theme (Wu et al., 2023).

Several alkaline ring complexes (>130 ring) are documented in the northeastern part of Africa that spread from Precambrian (~650 Ma) until Neogene age (~25 Ma, Serencsits et al., 1981; Mohamed, 1998). The alkaline rocks in Egypt form moderately low-volume magmatic assemblages in the form of ring complexes/dykes, plugs, and lava flows associated with alkali granitic/or syenitic rocks that were erupted after the subducted-related magmatism at the termination of the Neoproterozoic Era (650–500 Ma) until Late Cretaceous. Meneisy (1986) proposed three alkaline volcanic activities involving Early Triassic-Late Permian (230 ± 10 Ma), Late Jurassic-Early Cretaceous (140 ± 10 Ma), and Late Cretaceous (90 ± 10 Ma). Most of these phases are situated in the South Eastern Desert (SED), Egypt (Fig. 1a) that are strictly connected with deep-seated faults/fractures and shear zones (Mohamed 1998). Some of these alkaline ring complexes may comprise both extrusive (like basalts, trachytes, and rhyolites) and intrusive rocks (e.g. gabbros, syenites, and granites, Landoll et al., 1994; Mogahed, 2016). Their rock types with their relatively remarkable minerals have attracted the interest of numerous petrologists, due to their high enrichments in Nb, Ta, Zr, Y, Th, and Cu ore deposits (Hezagy et al., 2016).

The Natash volcanoes (NV) represent one of the largest lava fields (~560 km^2) in the SED that are located about 125 km ENE of Aswan (Fig. 1a). Several authors discussed the origin of the Natash volcanoes (Crawford et al., 1984; Mohamed, 1998; Abu El-Rus et al., 2016; Khalaf et al., 2018). No researches have been paid a consideration to the genetic affiliation between the Natash volcanoes and its plutonic counterparts (such as the Abu Khruq or El Kahfa ring complex in Egypt, south of Ak, Fig. 1a) in order to understand the whole magmatism during Mesozoic Era. Moreover, the process for Nb enrichment characterizing the alkaline magmas is discreet enigma. In this article, we present an integrated study in terms of zircon U-Pb dating, mineral chemistry, and whole-rock geochemical data for alkaline Natash volcanoes, aiming to (1) constrain the magma source and evolution of the alkaline volcanoes, (2) constrain the mechanisms responsible for Nb enhancement, and (3) propose a detailed framework for the geodynamic evolution and shed new light on the tectono-magmatic development of the Mesozoic magmatism.

Analytical procedures

The specimen preparation and XRF procedures followed the technique of Sano et al. (2016). In addition to the XRF analyses (Table 1), the rock powders of 19 specimens were used for analysis of trace elements by inductively coupled plasma-source mass spectrometry (ICP-MS). Trace element compositions were determined using a quadrupole Agilent 7700x ICP-MS instrument at the National Museum of Nature and Science, Japan (NMNSJ). Prior to ICP-MS analysis, whole-rock powders were dissolved using a HF–$HClO_4$–HNO_3 with ultimate dissolution in 2% HNO_3 plus 0.1% HF spiked with ^{115} In and ^{209} Bi.

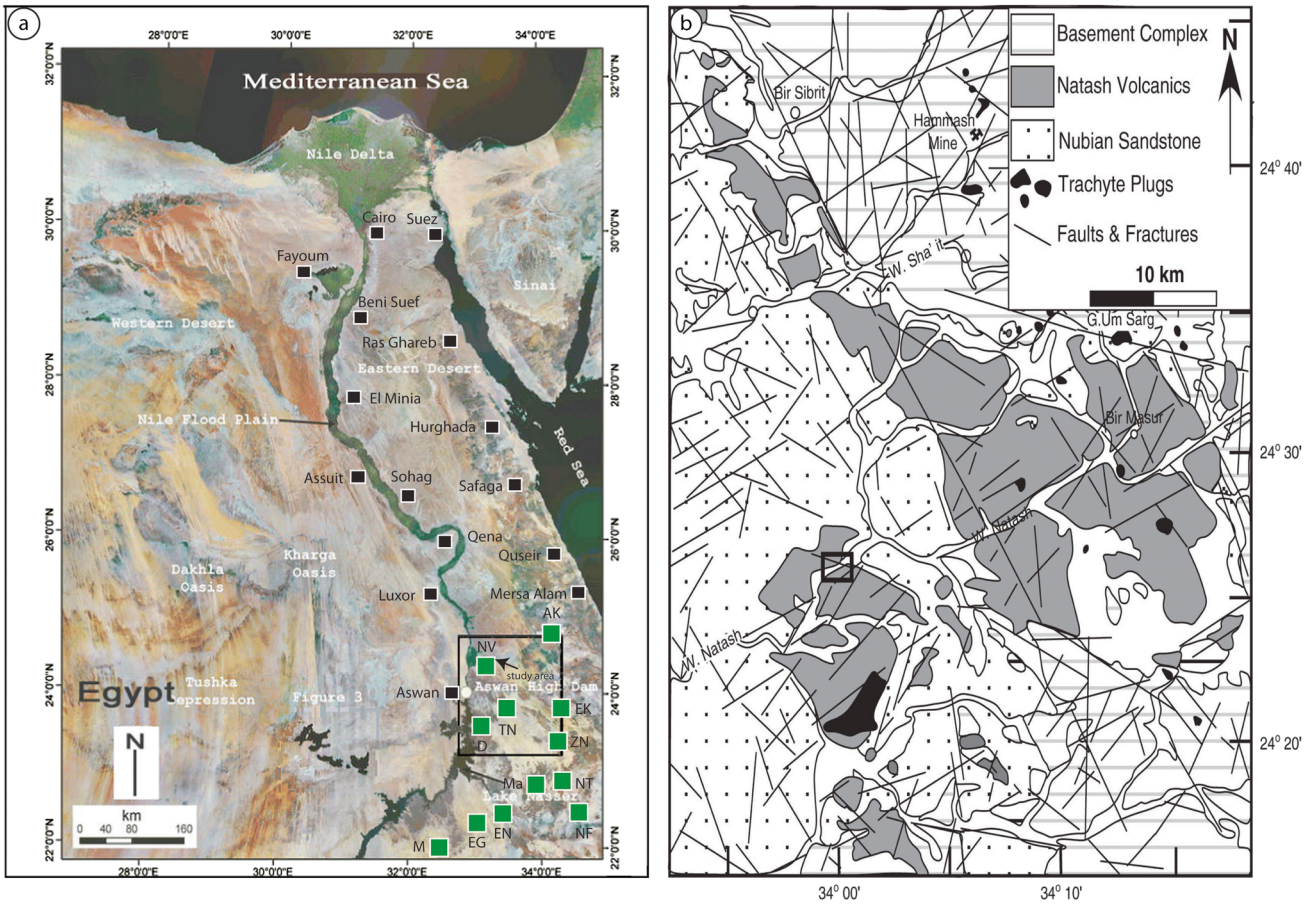

Fig. 1 Location of ring complexes and geological map of Wadi Natash. **a** Key map showing the distribution of the main ring complexes in the South Eastern Desert (SED), Egypt: NV, Natash volcanoes (study area); AK, Abu Khrug; ZN, Zargat Naam; TN, Tarbite North; D, Dahmit; NT, Nigrub El Tahtani; NF, Nigrub El Fokani; EN, El Naga; M, Mansouri; Ma, Malaadob. **b** Geological map of Natash volcanoes (modified after CONOCO 1987)

Analytical precision was appraised using the JB2 and JB2-recom as references. Polished sections for mineral compositions were perceived using a JEOL electron microprobe (JEOL JXA-8230) using 15-kV accelerating voltage, 15-nA beam current, and an analytical spot size of ~1 µm.

Five samples were chosen for zircon U-Pb dating. Full measures for zircon separation and U-Pb analyses are summarized (see Tsutsumi et al., 2012). The FCL zircon ($^{206}Pb/^{238}U = 0.1859$; Paces and Miller 1993) and NIST SRM standard glass were used as references. Scanning electron microprobe cathodoluminescence (SEM-CL) apparatus, JSM-6610 (JEOL), and a CL detector (SANYU electron) have been used for backscattered electron and cathodoluminescence (CL) images. U-Th-Pb isotopic analyses were carried out using LAICP-MS (Agilent 7700x with ESI NWR213 laser ablation system). Pb corrections for the concordia diagrams and for each age were made based on the Pb model planned by Stacey and Kramers (1975). All these analyses were made at NMNSJ.

Geological background

The Natash volcanoes represent one of the most common Mesozoic ring complexes and demonstrate explosive/extrusive low-volume monogenetic eruptions in the SED (Khalaf et al., 2018). These volcanoes are aligned in the NW-SE direction and situated between latitudes 24°15′–24°50′ N and longitude 33°40′–34°10′ E, unconformably overlying the Precambrian rocks and Nubia sandstone of Upper Cretaceous (Fig. 1b). The lava thickness attains 250 m at the eastern part of Wadi Natash, which declines to about 50 m at its western portion (Crawford et al. 1984). The NV appear in three ring structures that are exposed along Gaziret Khashm

Table 1 Major trace elements of Upper Cretaceous A-type Natash volcanoes, South Eastern Desert, Egypt

Element	N1	N2	N3	N4	N5	N6	N7	N8	N9	N10	N11	N12	N13	N14	N15	N16	N17	N18	N19	N20	N21	N22	N23	N24	N25	N26	N27	N28	N29	N30
SiO_2	41.56	45.32	46.05	49.36	49.61	49.47	50.46	52.60	55.3	55.5	55.5	52.9	56.7	57.4																
TiO_2	2.03	3.11	3.35	2.72	3.54	2.72	3.35	1.79	3.63	1.72	3.54	1.58	2.27	1.25	57.82	58.01	58.15	61.84	61.87	61.89	61.98	62.77	63.6	72.1	61.06	63.15	64.03	64.31	64.62	52.93
Al_2O_3	15.81	15.72	15.75	15.92	15.53	15.73	16.08	16.04	17.1	15.8	16.8	16.2	12.9	16.4	0.47	0.47	1.26	0.20	0.40	0.19	0.19	0.18	0.21	0.41	1.15	0.2	0.23	0.23	0.23	1.58
FeO	12.88	12.84	13.63	13.41	14.47	14.55	14.07	13.45	9.23	13.1	11.4	10.3	12.5	11.2	17.21	17.32	16.60	15.85	15.47	15.73	16.09	15.38	16.1	12.5	16.13	16.06	15.33	15.44	15.5	16.22
MnO	0.12	0.18	0.19	0.14	0.31	0.15	0.14	0.25	0.06	0.11	0.06	0.2	0.17	0.13	9.13	8.95	6.56	5.93	7.32	6.47	6.05	5.58	5.05	1.78	5.18	4.9	4.91	4.45	4.65	10.25
MgO	11.17	5.34	5.46	1.68	3.72	1.6	1.79	1.81	0.38	0.86	0.29	1.89	0.8	0.83	0.20	0.18	0.16	0.13	0.29	0.15	0.14	0.10	0.15	0.06	0.19	0.14	0.13	0.15		
CaO	12.75	8.18	8.21	4.81	4.01	5.22	4.60	3.41	2.82	3.08	1.93	5.19	4.08	1.41	0.45	0.48	0.68	0.57	1.50	0.64	0.36	0.62	0.12	0.19	0.64	0.1	0.17	0.31	0.17	0.2
Na_2O	1.76	3.73	3.83	6.22	7.05	5.16	6.47	5.91	7.75	5.3	8.92	5.27	6.12	7.98	2.73	2.79	3.94	2.11	0.50	1.98	1.35	2.28	1.23	1.74	2.38	1.18	1.06	1.36	0.24	1.89
K_2O	0.24	1.09	1.12	1.76	0.12	1.59	0.56	1.61	0.61	2.04	0.58	2.7	0.72	1.43	7.17	7.06	8.73	5.58	4.15	5.35	6.68	5.24	6.50	4.32	6.59	6.65	6.38	5.19	1.06	5.19
P_2O_5	0.01	0.79	0.87	2.09	0.62	1.84	0.75	0.74	0.68	0.72	0.60	0.74	1.75	0.36	3.29	3.16	0.62	4.74	5.64	4.87	5.08	3.94	5.01	4.95	3.11	5.02	5	5.76	5.18	5.27
LOI	1.30	3.98	2.00	2.02	1.56	2.3	2.13	2.57	2.69	2.2	1.01	3.25	1.79	1.79	0.18	0.19	0.40	0.02	0.09	0.03	0.03	0.04	0.04	0.03	0.34	0.03	0.05	0.03	5.82	2.7
Total	99.63	100	100	100	100	100	100	100	100	100	100	100	99.9	100	1.75	1.74	3.03	3.19	2.70	2.40	2.38	3.89	2.08	2.13	3.26	2.79	2.96	3.46	0.03	0.74
V	614	216	228	99	169	92	227	43	227	44	289	26	86	16	100	100	100	100	99.93	99.70	100	100	100	100	100	100	100	100	2.61	3.25
Cr	179	36	38	8	18	8	23	6	21	6	27	3	7	4															100	100
Co	61	54	55	46	46	45	45	38	27	35	30	23	39	38	7	7	14	3	10	2	3	2	4	10	16	3	3	3	2	26
Ni	150	17	17	0	2	0	10	0	4	0	3	0.3	0	0	2	2	3	1	4	11	1	4	0	2	3	1	2	1	1	3
Rb	4	17	17	22	2	22	8	20	14	40	10	38	10	17	16	16	17	10	7	5	10	12	7	3	13	9	7	17	5	23
Sr	172	658	634	776	127	886	323	567	401	598	290	658	592	657	2	1	2	4	4	0	5	7	5	7	3	5	5	5	5	0.3
Ba	14	229	222	612	4	672	199	591	219	631	141	798	196	1232	62	60	11	140	120	149	137	119	115	128	56	104	124	140	139	36
Y	11	27	27	36	36	39	39	42	36	54	35	39	35	51	418	499	454	52	230	60	62	51	41	22	940	24	19	45	29	595
Zr	15	263	222	291	230	369	264	258	312	485	258	390	249	433	825	908	202	113	2136	173	70	75	583	220	1898	532	48	42	45	798
Nb	0	50	38	44	47	67	50	49	42	81	48	84	53	79	63	61	66	114	131	124	122	138	104	98	56	115	100	109	107	39
La	---	39	---	---	---	63.44	---	---	---	77	---	57	---	---	653	667	486	1394	1297	1601	1661	1807	1159	1044	522	1147	1677	1567	547	390
Ce	---	88	87	137	99	141	104	142	101	162	100	125	124	160															179	83
Pr	---	10.45	---	---	---	17.07	---	---	---	19	---	15	---	---	95	95	99	249	233	256	252	283	225	162	92	201	175	178	---	57
Nd	---	43.24	---	---	---	70.48	---	---	---	77	---	66	---	---	---	---	---	133	128	145	167	159	134	---	---	---	---	---	---	126
Sm	---	8.97	---	---	---	13.7	---	---	---	15.5	---	13	---	---	194	196	170	277	323	299	298	327	285	298	---	---	---	---	---	15.86
Eu	---	2.89	---	---	---	4.74	---	---	---	5.63	---	4.94	---	---	---	---	---	34.7	35.75	37.28	37	42	36.4	---	---	---	---	---	---	66
Gd	---	8.03	---	---	---	11.8	---	---	---	13.5	---	11.5	---	---	---	---	---	126.8	133.8	136	135	153	133	---	---	---	---	---	---	13.4
Tb	---	1.16	---	---	---	1.65	---	---	---	2.07	---	1.65	---	---	---	---	---	25.5	27.7	27	27	31	25	---	---	---	---	---	---	4.94
Dy	---	5.97	---	---	---	8.11	---	---	---	11.2	---	8.4	---	---	---	---	---	2.97	7.39	3.05	3.14	3.56	3.92	---	---	---	---	---	---	11.5
Ho	---	1.08	---	---	---	1.44	---	---	---	2.15	---	1.5	---	---	---	---	---	23.5	26.4	24.4	24.1	29	21.2	---	---	---	---	---	---	1.65
Er	---	2.8	---	---	---	3.72	---	---	---	5.96	---	3.96	---	---	---	---	---	3.87	4.49	4.07	4.08	4.85	3.49	---	---	---	---	---	---	8.4
Tm	---	0.35	---	---	---	0.46	---	---	---	0.8	---	0.52	---	---	---	---	---	21.79	25.71	23	23.05	27	19.2	---	---	---	---	---	---	1.5
Yb	---	2.1	---	---	---	2.7	---	---	---	4.9	---	3.2	---	---	---	---	---	4.19	4.91	4.48	4.48	5.18	3.71	---	---	---	---	---	---	3.96
Lu	---	0.3	---	---	---	0.39	---	---	---	0.72	---	0.48	---	---	---	---	---	11.8	13.7	12.6	12.6	14.2	10.5	---	---	---	---	---	---	0.52
Hf	---	5.95	---	---	---	6.67	---	---	---	11.5	---	8.92	---	---	---	---	---	1.61	1.91	1.7	1.7	1.9	1.45	---	---	---	---	---	---	3.2
Ta	---	2.89	---	---	---	3.78	---	---	---	4.79	---	4.66	---	---	---	---	---	10	13	11	11	12	9.2	---	---	---	---	---	---	0.48
Tl	---	0.06	---	---	---	0.03	---	---	---	0.03	---	0.04	---	---	---	---	---	1.39	1.96	1.43	1.47	1.59	1.33	---	---	---	---	---	---	8.92
Pb	0.8	2.1	18	21	22	2.82	3	3.8	3.4	5.83	3.2	3.31	2.2	3.4	---	---	---	36.2	32.9	36	38.2	40	22.9	---	---	---	---	---	---	4.66
Th	0.7	3.49	3.4	5	3.6	5.27	4.3	5.9	4.4	7.38	3.5	6.36	4.4	7.6	---	---	---	15.08	13.2	14.63	15.54	16.58	11.9	---	---	---	---	---	---	0.04
U	---	1.05	---	---	---	1.59	---	---	---	2.37	---	1.23	---	---	---	---	---	0.15	0.16	0.15	0.39	0.16	0.13	---	---	---	---	---	11.3	3.31
Ga		24.3				31.3				33.3		28.2			7.4	7.8	7.6	9.46	4.03	13	17.4	5.31	12.9	4	5.3	12.1	13.7	11.3	---	6.36
Eu/Eu*	---	1.05	---	---	---	1.16	---	---	---	1.2	---	1.21	---	---	9.9	10.7	9	21.75	15.08	24.5	24.44	24.65	16.3	18.2	8.8	15	17.6	17.2	---	1.23
La/Nb	---	0.78	---	---	---	0.95	---	---	---	0.95	---	0.68	---	---	---	---	---	6.81	3.76	6.13	4.82	8.18	4.74	---	---	---	---	---	---	28
Zr/Nb	---	5.26	---	---	---	5.51	---	---	---	5.99	---	4.64	---	---				52	51	49	47	50.5	44.9						---	0.69
La/Sm	---	4.35	---	---	---	4.63	---	---	---	4.97	---	4.38	---	---	---	---	---	0.38	0.84	0.36	0.38	0.37	0.52	---	---	---	---	---	---	4.70
La/Yb	---	18.57	---	---	---	23.5	----	----	----	15.7	----	17.8	----	----	---	---	---	0.53	0.55	0.57	0.66	0.56	0.60	---	---	---	---	---	---	4.25
Nb/Th	---	14.32	11.18	8.8	13.06	12.71	11.63	8.31	9.55	10.9	13.7	13.2	12	10.4	---	---	---	5.60	5.57	6.25	6.59	6.39		---	---	---	---	---	---	17.8
															---	---	---	5.21	4.62	5.37	6.19	5.13	5.36	---	---	---	---	---	---	13.1
															---	---	---	13.3	9.84	13.2	15.2	13.3	14.6	---	---	---	---	---		
															9.50	8.88	11	11.5	15.5	10.5	10.5	11.5	13.8	8.90	10.5	13.4	9.94	10.3		

Major/trace elements were detected by X-ray fluorescence (XRF)

Rare earth elements (REE) were detected by inductive coupled plasma-mass spectrometer (ICP-MS)

Major elements in wt%; trace elements in ppm

(-) not analysed

FeO, total iron as ferrous; *LOI*, loss on ignition

Natash, Western Ghorfa, and Gabal El Ghorfa (Fig. 2a, Saleh et al., 2021). The Gaziret Khashm Natash occurs as a horse shoe-ring structure attaining 0.6 km in width. It is characterized by lava flows and volcaniclastic sediments (Fig. 2d), while the second occurs as an incomplete ring with 0.7 km in width, consisting chiefly of three sequences of lava flows with gradational contacts (Fig. 2c). The volcanoes in the Gaziret Khashm Natash are dispersed in WNW–SSE-trending belts that are crossed by the NNE–SSW right lateral faults (Saleh et al., 2021), which may be linked to fissure eruption. Gabal El Ghorfa forms a ring dyke of trachytic composition with a width of 1 km. The Rb/Sr and K-Ar dating gave an eruptive age ranging from 104 ± 7 to 85.6 ± 3 Ma for the volcanic activity in Wadi Natash (El-Shazly and Krs, 1973; Hashad and El-Reedy, 1979). The Natash volcanoes form hilly outcrops with stratification (Fig. 2b). Based on the interpretations of Khalaf et al. (2018), the Natash volcanoes at Gaziret Khashm Natash occur as tuff cone/or tuff ring which experienced Hawaiian-Vulcanian eruptive style of purely magmatic phase that followed an initial explosive phreatomagmatic phase which was sporadically fed by trachyandesitic and trachytic magmas. The NV encompass a comprehensive array of volcanic products including volcano-sedimentary deposits, lava flows, and subvolcanic intrusions, forming three rock sequences. The initial sequence occurs as cone-shaped edifice having 2 km in diameter and involves ignimbrites (facies "A"), lapilli-tuffs (facies "B"), hyaloclastites (facies "C"), and conglomerates (facies "D"). The latter signifies unconformity surface, separating early formed volcaniclastics (explosive stage) from overlying effusive lava flows (facies "E") along sharp contact. The second sequence includes multicycles of massive

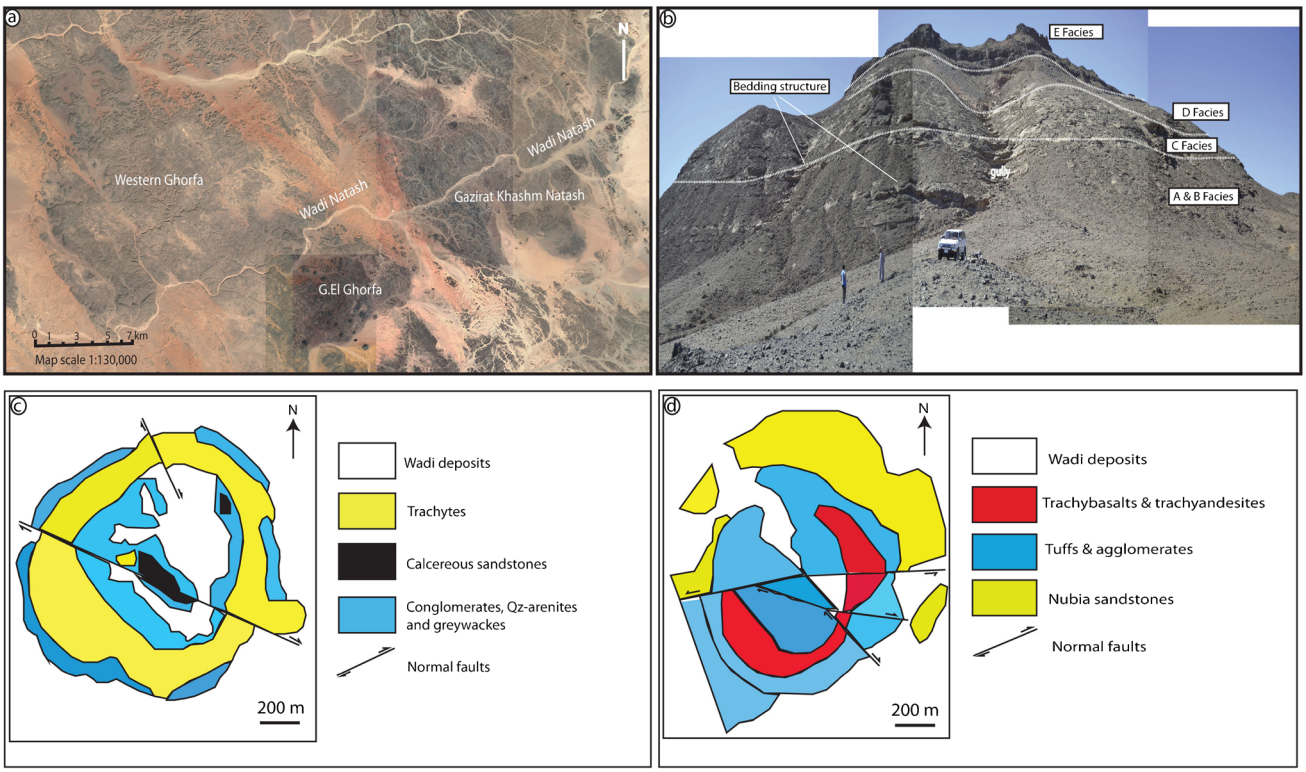

Fig. 2 **a** Landsat image of Wadi Natash volcanoes. **b** Photo showing volcanic stratigraphy involving A-B facies (ignimbrite and lapilli-tuff), C facies (hyaloclastites), facies D (conglomerates), and E facies (lava flows). **c**, **d** Geological maps of Gabal El Ghorfa ring dyke and Gaziret Khashm Natash, Wadi Natash, SED, Egypt (Saleh et al. 2021)

lava flows, up to 20 m in thickness, and displays two perpendicular sets of joints along with extremely vesicular exterior, occasionally intercalated with the Nubian sandstones. Subrounded mantle xenoliths are observed in the basaltic lavas, as has been previously detected by many authors (Abu El-Rus et al. 2016, 2018). The third sequence is represented by subvolcanic intrusive plugs which occur as steep-slope massive bodies, attaining up to 100-m height, and its thickness varies from 5 to 10 m. Columnar joints and screes/or talus-rich upper surfaces characterize the intrusive plugs.

Abundant ring complexes are delineated by N60°E- to N30°W-striking lineaments in the SED that were controlled by pre-existing deep crustal faults/fractures within the basement complex (Garson and Krs, 1978; Omar et al., 1987). These complexes were formed during diverse magmatic stages that happened between 230 and 84 Ma in an intraplate environment (Meneisy, 1986). Examples of these complexes are El Kahfa ring complex (ERC), El Gezira (229–230 Ma), El Naga (84–220 Ma), El Mishbeh (141–184 Ma), Shabih (191 ± 7 Ma), Nigrub El Tahiani (139.7 ± 9 Ma), and Nigrub El Fogani (132–142 Ma). ERC is composed of essexitic gabbros and syenitic rocks as well as extrusive rocks of trachyte, rhyolite, and basanite (Hegzay et al. 2016) that are emplaced at 92 ± 5 Ma, belonging to the Upper Cretaceous ring complexes (Serencsits et al., 1981; Lutz et al., 1988), whereas other ring complexes consist of alkali syenite and granite (Hashad, 1994).

Petrography

The mantle xenoliths recorded in Natash volcanoes are coarse-grained and composed of clinopyroxene crystals. The latter are holocrystalline, colourless, and subhedral crystals, showing hypidiomorphic equigranular texture and exsolution lamellae (Fig. 3a, b). The main eruptive products of the NV are represented by mafic, intermediate, and felsic types.

Mafic rocks

These rocks are fine-grained and black in colour with characteristically porphyritic textures. They include ~30% subhedral to anhedral phenocrysts of olivine, clinopyroxene, and plagioclase crystals (Fig. 3c–z). Olivine crystals occur as subhedral to anhedral phenocrysts with distinctive resorption, fractures, embayment, rounded rims, and

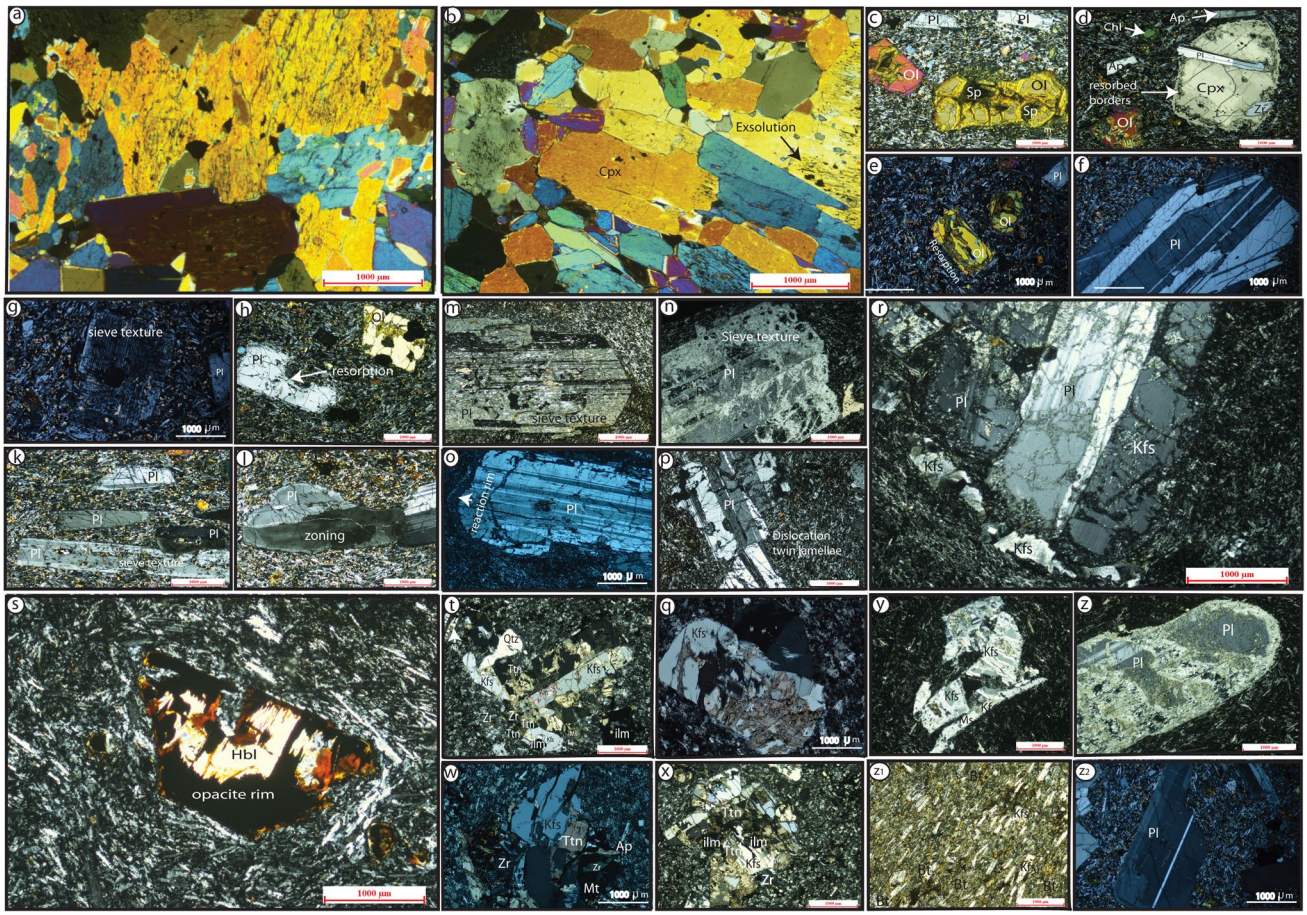

Fig. 3 Photomicrographs showing the main petrographic characters of the Natash volcanoes. **a**, **b** Photomicrographs showing the subhedral crystals of clinopyroxene forming mantle xenolith. **c** Altered and fractured subhedral-anhedral crystals of olivine (Ol) embedded in a fine matrix. **d** Prismatic euhedral crystals of clinopyroxene with resorption and fine cracks. Notice plagioclase subophitically enclosed with clinopyroxene phenocryst. **e** Resorption along olivine rims. **f** Complex zoning and twinning in plagioclase phenocrysts. **g** Sieve-rich core in plagioclase phenocrysts. **h** Grains of resorbed plagioclase (Pl) and altered olivine (Ol) set in a fine matrix. **k**, **l** Fine oscillatory zoning observed in plagioclase crystals. **m** Core-rim sieve textures in twinned plagioclase phenocrysts. **n** Sieve-rich rims in plagioclase phenocryst. **o** Reaction rims along the borders of twinned plagioclase phenocryst. **p** Deformed twinned plagioclase phenocryst showing dislocated twin lamellae. **r** Antirapakivi texture consisting of K-feldspar (Kfs)-encircled plagioclase (pl). **s** Black opacite rims (encircle) amphibole borders. **t** Altered K-feldspar associated with accessory titanite (Ttn), apatite (Ap), zircon (Zr), and ilmenite (ilm). **q** Simple twinning observed in potash feldspar (Kfs). **w**, **x** Altered K-feldspar (Kfs) with accessory minerals involving titanite (Ttn), sphene (Sph), and ilmenite (ilm). **y** Intensive degree of kaolinization affects K-feldspar (Kfs) with corrosive borders. $\mathbf{z_1}$ Hydrothermal biotitization observed along feldspar borders. $\mathbf{z_2}$ Complex zoning in plagioclase phenocrysts

iddingisitization especially along their borders and cleavages. Spinel grains occur as inclusions in olivine crystals (Fig. 3c). The crystals of clinopyroxene occur as colourless subhedral crystals and show resorption, embayment, and sieve textures particularly along their rims. They contain zircon, apatite, and Fe-Ti oxides as inclusions and show ophitic texture with lath-shaped plagioclase (Fig. 3d). Plagioclase crystals are fresh, subhedral, and lath-shaped, with 0.5 mm in length. Simple twinning and oscillatory zoning with resorption and sieve texture characterize most plagioclase phenocrysts (Fig. 3g–l). The groundmass is composed of lath-shaped feldspar, olivine, pyroxene, and opaques with typically fluidal texture.

Intermediate-felsic rocks

Intermediate rocks of trachyandesitic to trachytic in composition are characterized by enrichment of crystals (>50%), displaying coarse to microporphyritic textures displaying hypocrystalline and trachytic fabric. They contain mineral associations composed of plagioclase and alkali feldspar with subsidiary biotite, aegirine, and amphibole. Their crystals display a wide range in size, varying from megacrysts (>3 mm) through microphenocrysts (0.3–3 mm) to microliths (<0.3 mm). Plagioclase crystals are chiefly subhedral to anhedral megacrysts and phenocrysts as well as lath-shaped outlines in groundmass (Fig. 3m–r). They

involve melt inclusions and display simple and lamellar twinning as well as composite zoning (Fig. 3n, o). Intensive fractures, bending in twin lamellae, and partial to complete replacement by kaolinite and white mica characterize plagioclase feldspar (Fig. 3p). The latter show marks of disequilibrium features such as fine and coarse-sieve textures, embayment, resorption, dissolution, rounded rims (Fig. 3m, n), and rapakivi/antirapakivi textures (Fig. 3r). Amphibole phenocrysts are dark brown in colour and subhedral crystals and form six-sided or prismatic shape with characteristically simple twinning and colour zoning. They show reaction rims and partial to complete replacement by mica and opaques (Fig. 3s). The phenocrysts of aegirine are subhedral crystals and dark green in colour showing simple twinning and partial replacement by chlorite. Alkali feldspars are subhedral to anhedral twinned crystals and show moderate alteration to sericite and kaolinite (Fig. 3t–y). Accessory zircon, apatite, titanite, rutile, and magnetite along with epidote (allanite) and mica are observed (Fig. 3w, x). The grains of titanite form as subhedral to euhedral crystals and occur as inclusions in the alkali feldspar (Fig. 3x). Oscillatory zoning and glass inclusions along core and rim of plagioclase crystals forming sieve textures are common (Fig. 3z, z_2). The groundmass is aphyric and consists of lath-shaped plagioclase, alkali feldspars, mica, biotite flakes encircled the feldspar laths (Fig. $3z_1$), and grains of magnetite and ilmenite demonstrating pilotaxitic and fluidal texture (Fig. $3z_1$, z_2). The subvolcanic plugs display similar texture and mineral assemblages to those in trachyandesites and trachytes. Alkali feldspar, quartz, and biotite with allanite, zircon, and Fe-Ti oxides characterize the felsic rocks. The quartz phenocrysts are anhedral crystals and show patchy outline.

Mineral chemistry

We analysed olivine and opaques from mafic rocks and plagioclase from intermediate rocks. All their compositional data are given in the supplementary Tables 1 and 2.

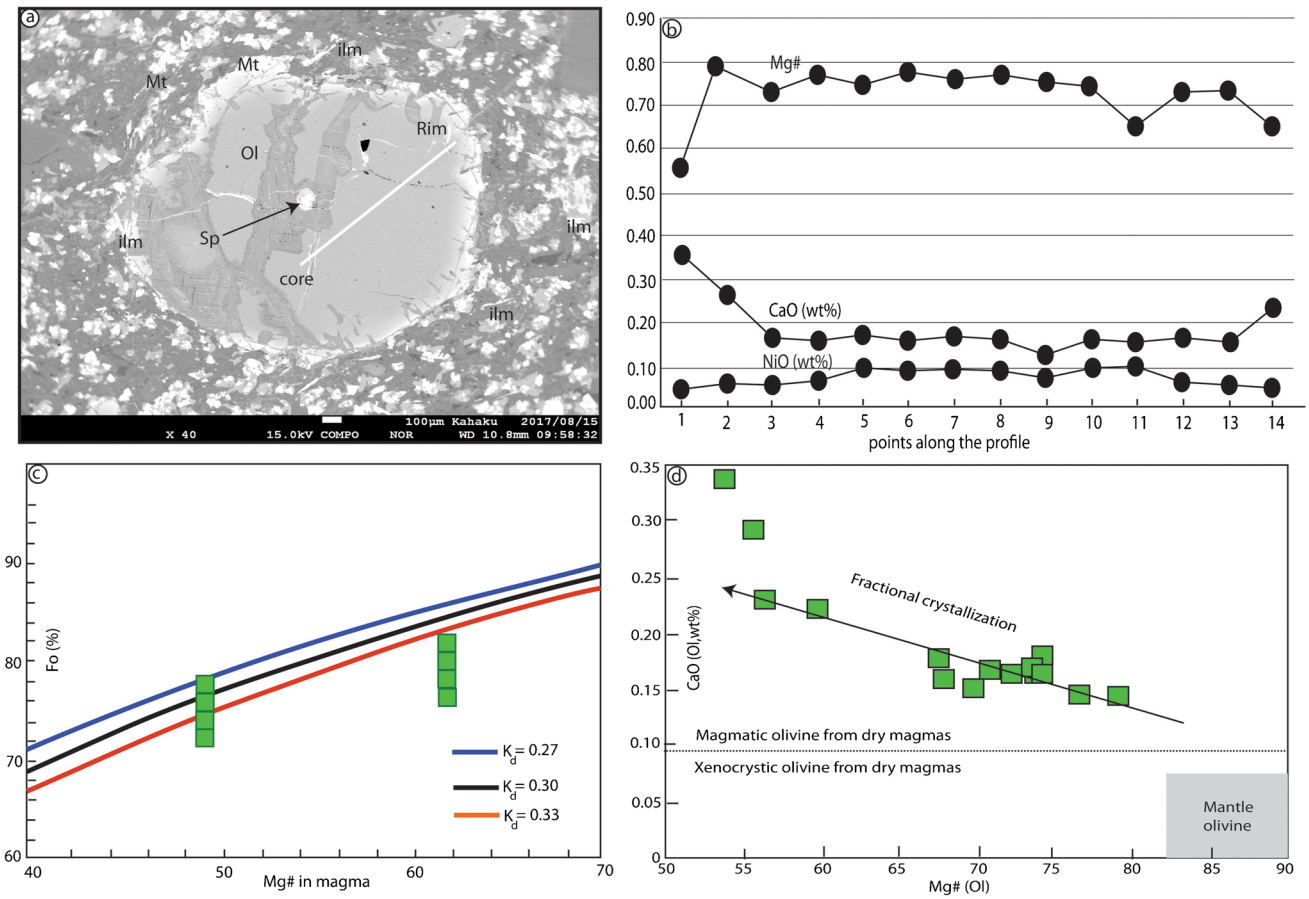

Fig. 4 Mineral compositions in the olivine phenocrysts. **a** Normal zoning pattern in rounded olivine with spinel (Sp) as poikilitic inclusion. **b** Mg#, CaO, and NiO variations vs. Fo content for olivine crystals. **c** Fo content of olivine phenocrysts vs. whole-rock compositions (Mg#). **d** CaO content of olivine versus Fo content of olivine. The solid line separates magmatic and xenocrystic olivine in dry mafic magmas on the basis of CaO content (Foley et al. 2013)

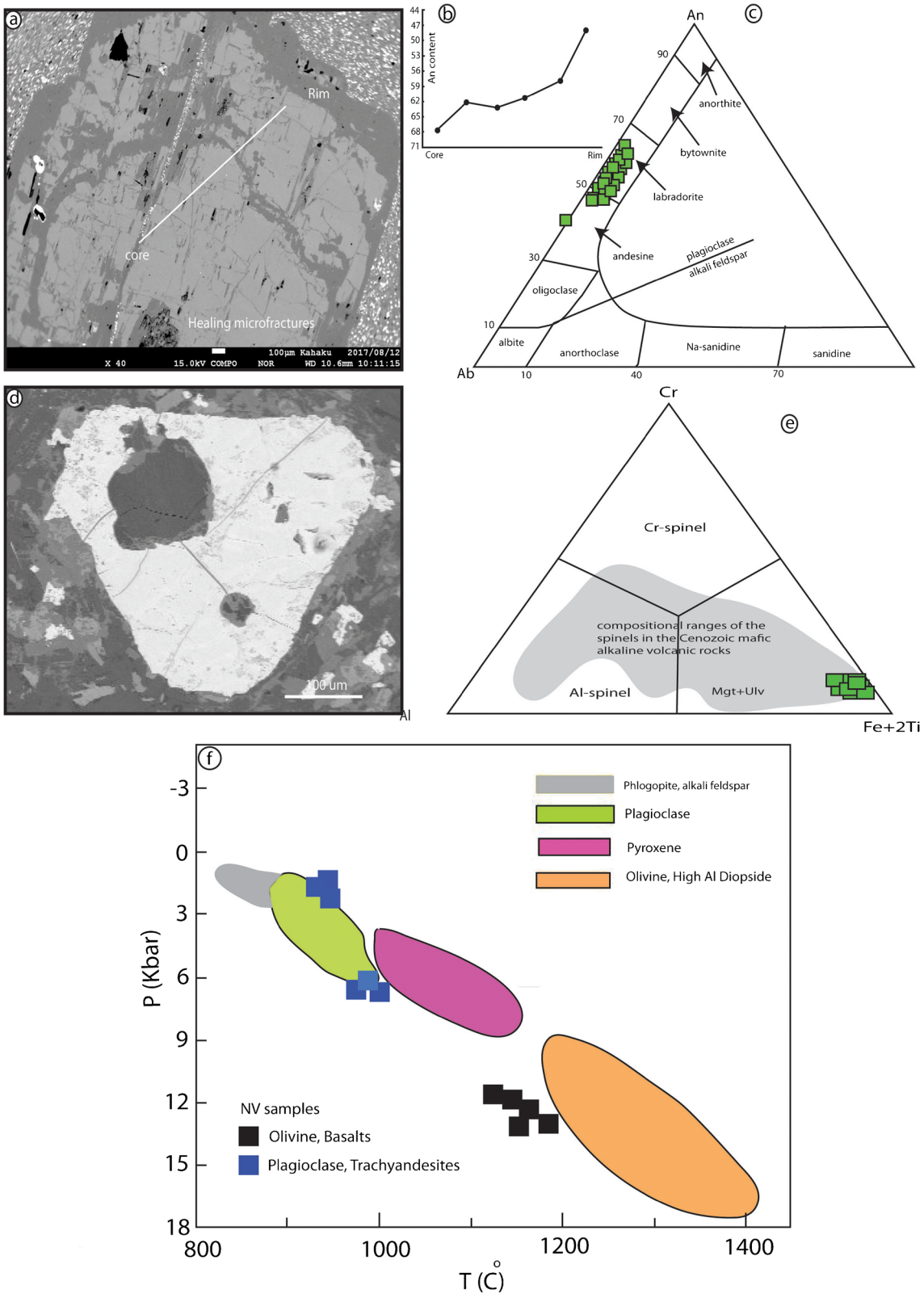
a
Rim
core
Healing microfractures
100µm Kahaku 2017/08/12
X 40 15.0kV COMPO NOR WD 10.6mm 10:11:15
b
An content
Core
Rim
c
An
anorthite
bytownite
labradorite
andesine
plagioclase
alkali feldspar
oligoclase
albite
anorthoclase
Na-sanidine
sanidine
Ab
d
100 um
Al
e
Cr
Cr-spinel
compositional ranges of the spinels in the Cenozoic mafic alkaline volcanic rocks
Al-spinel
Mgt+Ulv
Fe+2Ti
f
Phlogopite, alkali feldspar
Plagioclase
Pyroxene
Olivine, High Al Diopside
NV samples
Olivine, Basalts
Plagioclase, Trachyandesites
P (Kbar)
T (C°)

◂**Fig. 5** Mineral compositions in the plagioclase phenocrysts. **a** Subhedral plagioclase showing zoning and resorption with characteristic healing microfractures. **b** The variation of An content along core-rim of plagioclase crystals. **c** Feldspar compositions. **d** Octahedral form of spinel crystals. **e** Iron-titanium-rich spinels. The range of the spinels of other Cenozoic mafic lavas is also shown (Cucciniello et al. 2018). **f** Thermobarometric estimations for the minerals of the Natash volcanoes using equations of Putirka (2008). Field boundaries for the calculated P-T stability of olivine, pyroxene, plagioclase, phlogopite, and alkali feldspar characterized alkaline Damavand volcano (after Eskandari et al. 2018)

Olivine

Olivine phenocrysts are ubiquitous in mafic rocks (Fig. 4a). The Fo content declines from cores (Fo_{77-71}) to rims (Fo_{65-60}), demonstrating normal growth zoning (Fig. 4b). The olivine crystals display fluctuation in element concentration. They have increasing CaO (from 0.16–0.27 to 0.23–0.35 wt%) and decreasing Mn (from 0.74–0.58 to 0.25–0.45 wt%), NiO (0.07–0.6 to 0.01–0.04 wt%), and Al_2O_3 (from 0.04–0.05 to 0.01–0.03 wt%) from their cores to rims (Fig. 4b). The contents of CaO reveal that olivine crystals were formed from magmas (i.e. antecrysts) rather than lithospheric mantle peridotite–derived xenocrysts (Fig. 4d, Foley et al., 2013).

Plagioclase feldspar

The crystals of plagioclase are recorded in both mafic and intermediate rocks, displaying complex zoning (Fig. 5a). Their An contents (100 × Ca/(Ca+Na) in mole) range from 65 at the core to 45 at the rim, indicating labradorite (An_{70}) to andesine (An_{45}) in composition with no alkali feldspar (Fig. 5b, c). The K_2O, MgO, and FeO_T contents are low and do not display substantial core to rim variations, fluctuating from 0.3 to 0.6, 0 to 0.1, and 0.3 to 0.7 wt%, respectively, in the plagioclase feldspar.

Spinel

Spinels are found as inclusions in olivine crystals with euhedral octahedral shape (Fig. 5d). They are Ti- and Fe-rich (TiO_2 = 25–27 wt%, FeO = 61–65 wt%) with a homogeneous interior. The Cr_2O_3 and MnO contents range from 0.6 to 0.83 wt% and from 0.77 to 2.89 wt%, respectively. Their crystals have a limited variation in Al_2O_3 concentration (from 2.15 to 2.65 wt%), whereas MgO and NiO attain nil values. The enrichment of both Ti and Fe in the studied spinels reflects ulvöspinel composition (Fig. 5e).

Geothermobarometry

Olivine, plagioclase, and Fe-Ti phases have been used as geothermobarometers in order to evaluate the pressures, temperatures, and crystallization depths at which the magma stagnation regions were situated. The selected minerals advocate that the whole rock characterizes the melt composition wherever the minerals were formed (Coote and Shane, 2018). The method of Roeder and Emslie (1970) has been used (Fig. 4c) in order to test whether the Fo content of the olivine might be in equilibrium with a composition of the whole-rock liquid, relying on the apportioning of Fe-Mg between olivine and liquid which equals to $^{ol\text{-}Liq}D_{Fe\text{-}Mg}$ between 0.27 and 0.33 ± 0.03 underneath pressure <2–3 GPa (Roeder and Emslie, 1970). Olivine-melt thermometer (Putirka et al., 2008, Eq. 22) regulated for hydrous systems with its standard error of estimate (SEE) of about ±29 °C (Putirka, 2008) has been used. The Fo contents of the zoned olivine phenocrysts (Fo_{77-60}) are not in equilibrium with whole-rock liquid having Mg#62 (Fig. 4c), but equilibrium with the compositional mafic melt having Mg#50 with its K_D (Fe-Mg) equals to 0.234. Following the equations of Putirka (2008), a pressure of 1.3 GPa and a temperature of 1154 °C have been computed from the composition of olivine cores (Fo_{77-71}), declining to a pressure of 1.25 GPa and a temperature of 1136 °C for olivine rims (Fo_{65-60}). These calculations overall designate that zoned olivines with Fo_{77-60} equilibrated with Mg#50 host melts at 1.3–1.25 GPa (53–43 km) and 1154–1136 °C. Plagioclase-melt equilibrium can be used as thermobarometers and hygrometers which are regulated for hydrous systems with Kd_{plag} (K_D = 0.10 ± 0.05, T < 1050 °C) and SEE at pressure of ±2.47 kbar and a temperature of ±36 °C as well as H_2O content with a SEE of ±1.1 wt% (Putirka, 2008, Eq. 24a and 25a). A temperature of about 1048 to 980 °C and a pressure of about 0.76 to 0.26 GPa (26–9 km) were supposed for the plagioclase feldspar (An_{70-45}), which refer to the middle crustal depth (Murcia et al. 2019) along with crystallization of Fe-Ti oxides at 937–904 °C. By using the plag-melt hygrometer (Putirka 2008), the contents of H_2O melt are restricted between 1.5 and 2.3 wt%. All these data reflect that there are two storage zones beneath the NV: a deep zone at depths of ~53–43 km and a shallow crustal zone at depth of ~26–9 km.

SHRIMP U/Pb zircon geochronology

Zircon grains were chosen from the intermediate and felsic rocks for SHRIMP U/Pb dating. Five analyses on 20 zircon grains were done (supplementary Table 1) and shown in histogram (Fig. 6a) and Tera-Wasserburg diagrams (Fig. 6b). The length of these crystals ranges from 100 to 300 µm.

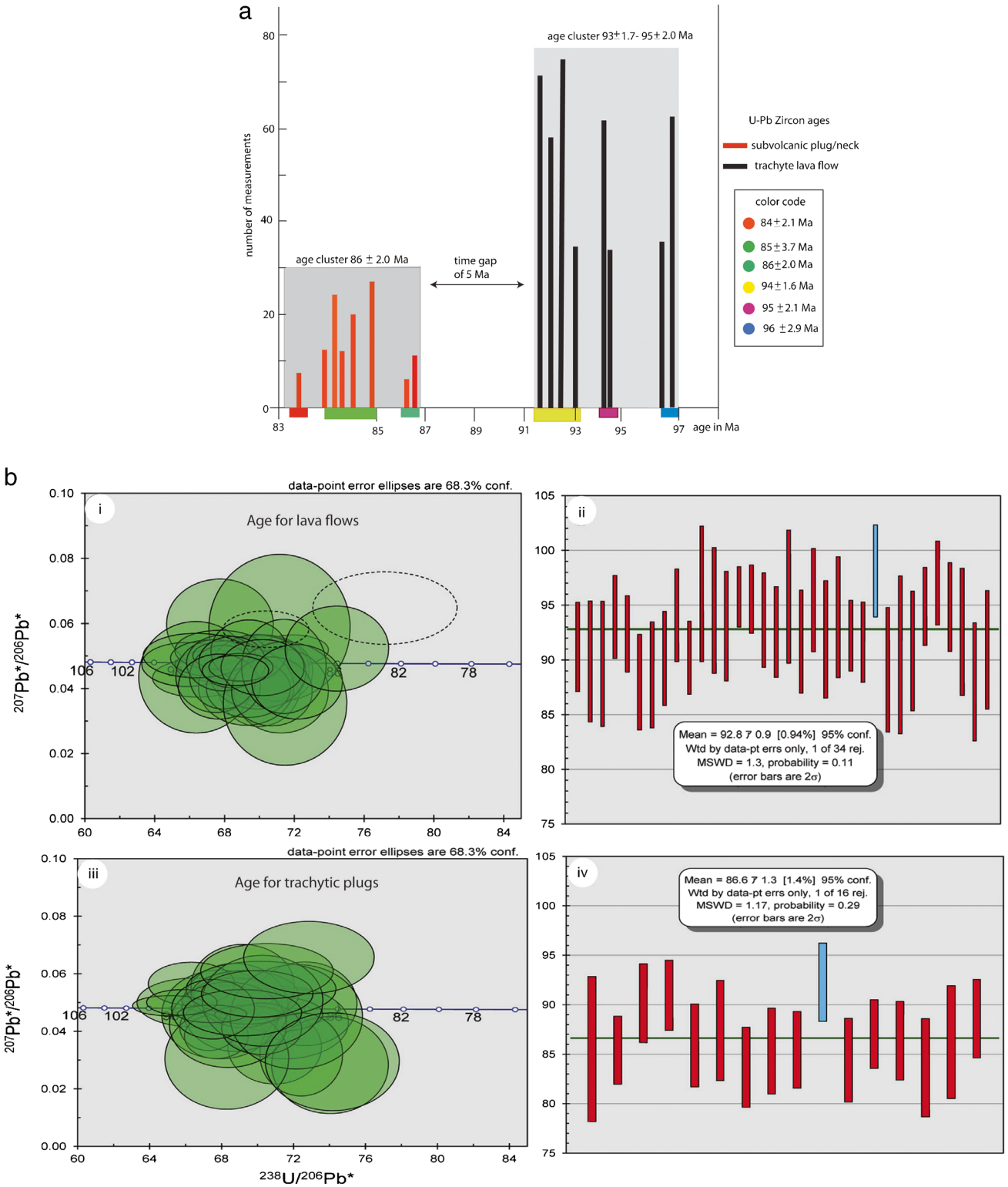

Fig. 6 U-Pb age dating of the Natash volcanoes. **a** Histogram illustrating U-Pb age for the Natash volcanoes. **b** Tera-Wasserburg U-Pb concordia diagrams (i and ii for trachyandesitic/trachytic flows and iii and iv for trachytic plugs

Euhedral-subhedral short prisms and transparent to translucent with no inclusions characterize the investigated zircon crystals, exhibiting generally magmatic oscillatory and sector zoning. All the results have been revealed that zircons selected from trachyandesitic/trachytic flows have U/Pb ages of 92–97 ± 0.9 Ma (n = 8, MSWD = 1.3/1.07) (Fig. 6b (i, ii)), while the youngest U/Pb ages give a period of 81–87 ± 1.3 Ma (n = 8, MSWD = 1.17) (Fig. 6b (iii, iv)) for trachytic plugs (Khalaf et al. 2018). This weighted average $^{206}Pb/^{238}U$ age denotes that the age of the NV is reliable with the formerly registered ages of the NV and syenite-granite suites of Abu Khrug and El Kahfa ring complexes (93–85.6 ± 3 Ma, El-Shazly and Krs, 1973; Hashad and El Reedy, 1979). Recently, Abu El-Rus et al. (2019) reported the occurrence of Precambrian zircon xenocrysts with U/Pb ages of 681 Ma in some trachyte plugs, typical for Egyptian basement rocks (~700 Ma). The bimodal ages documented by zircons (681 vs. 92 Ma) propose a wide time break (>500 Ma) between the termination of the Neoproterozoic Era and the beginning of unique magmatism in Wadi Natash area during Upper Cretaceous period.

Whole-rock geochemistry

Most rock specimens have mildly enriched LOI contents (>2 wt%), accredited to secondary minerals like kaolinite, white mica, chlorite, and carbonate. REEs and HFSEs (Zr, Nb, Y) are deliberated as immobile, owing to low correlation coefficients (>0.85). The LILEs (such as K, Rb, Ba, and Sr) have been exaggerated to various degrees by metasomatism or metamorphism. The slightly enriched contents of LOI of the Natash specimens probably propose the mobilization of LILEs. So, the immobile elements and its ratios as well as Ti, Ta, and Th elements have been used for geochemical and petrogenetic interpretations. On the Nb/Y vs. Zr/Ti diagram (Fig. 7a), the samples of the NV display a wide compositional array extending from basalts through trachyandesites-trachytes to phonolites-comendites that were formed within plate regime (Fig. 7c). Trachyandesitic/trachytic rocks contain high Zr (522–1807 ppm), Nb (92–283 ppm), Y (58–79 ppm), Rb (60–140 ppm), Ba (70–1889 ppm), Ta (11–16 ppm), Th (16–21 ppm), and U (4–8 ppm) concentrations and

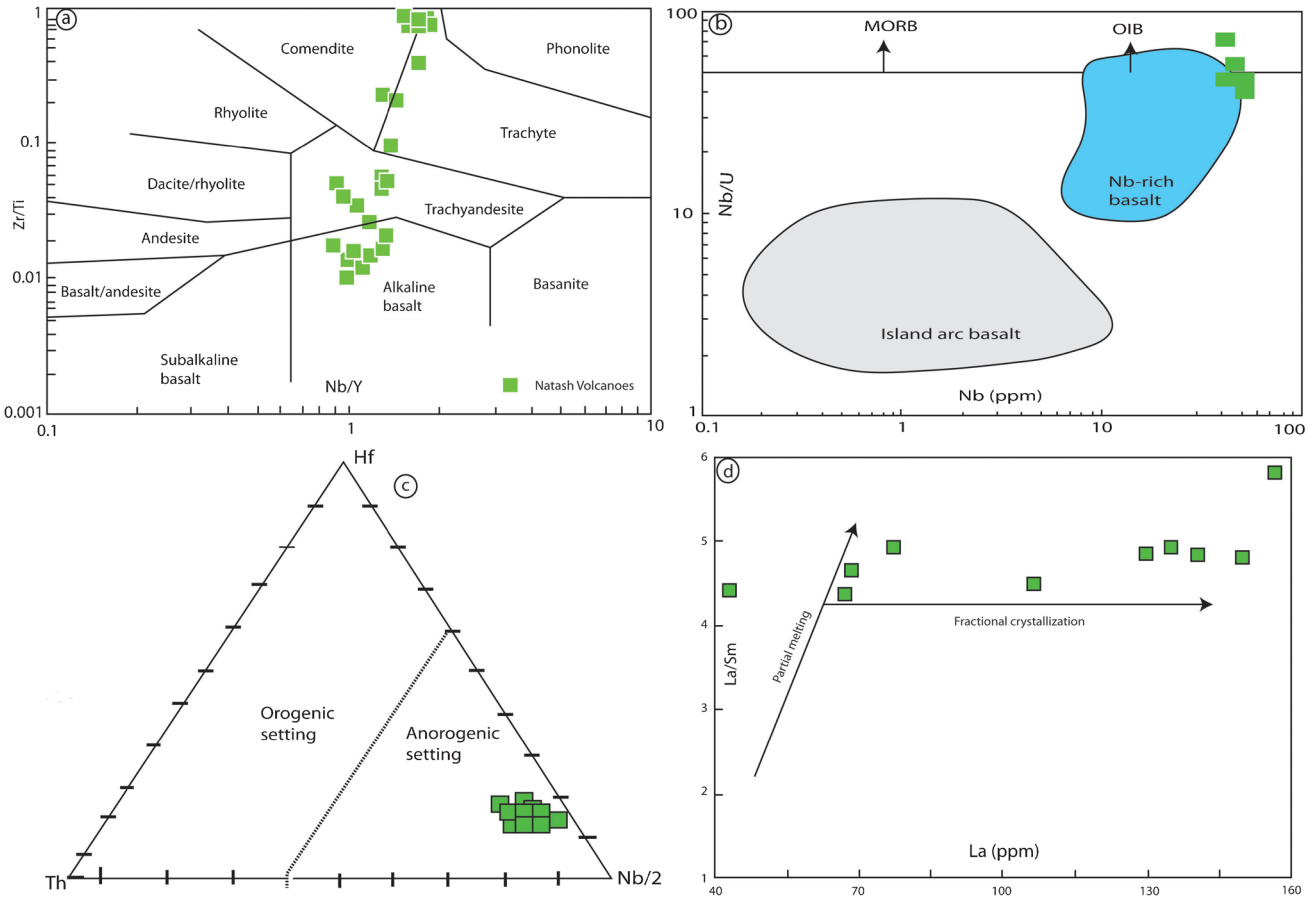

Fig. 7 Geochemical characteristics of the Natash volcanoes. **a** Zr/Ti vs. Nb/Y diagram (after Winchester and Floyd 1976). **b** Nb/U versus Nb (Xu et al. 2016). **c** Hf-Nb/2-th ternary diagram for distinguishing between orogenic and anorogenic setting. **d** La (ppm) vs. La/Sm binary diagram showing fractional crystallization and partial melting path

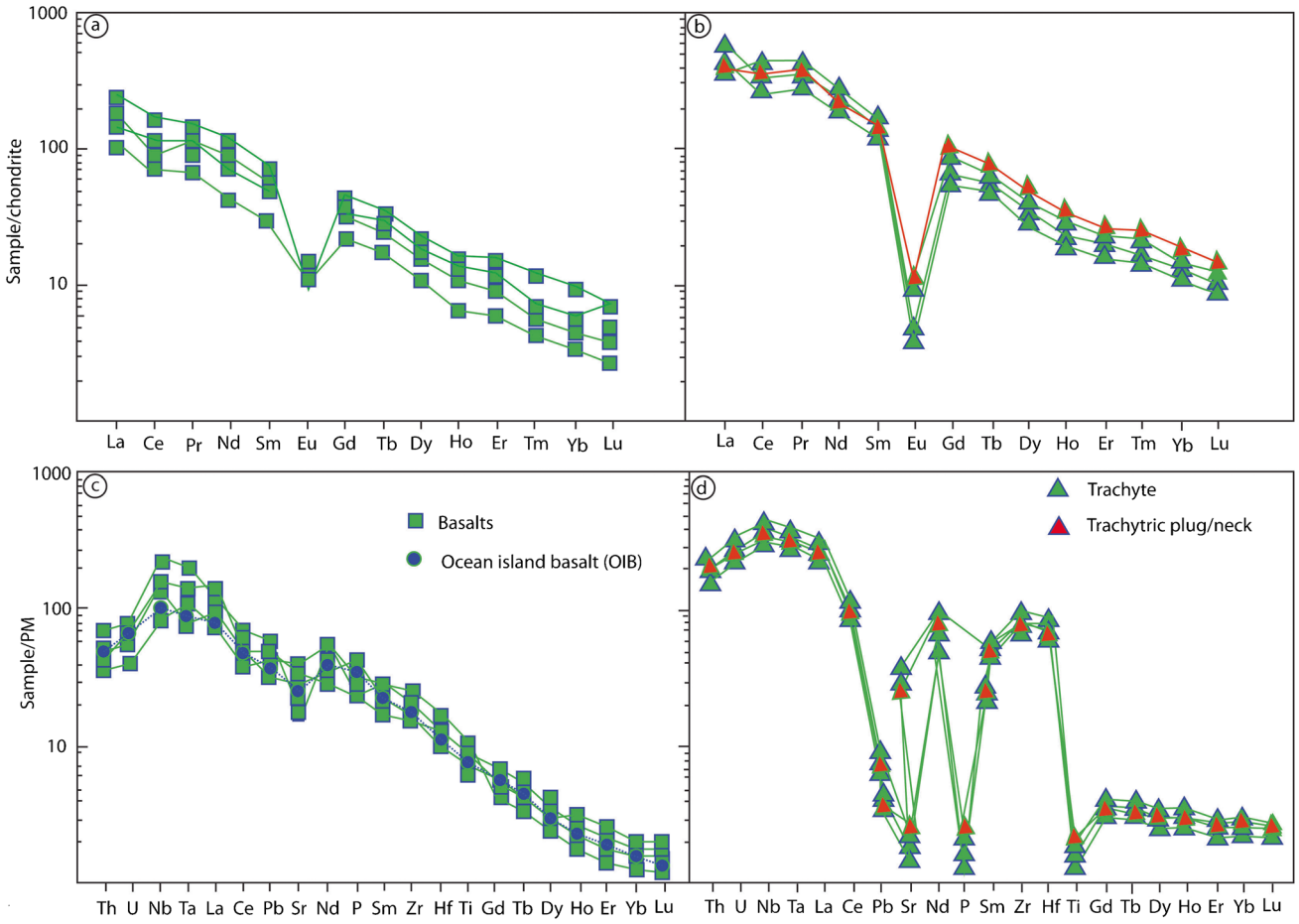

Fig. 8 Trace element normalization diagrams. Chondrite-normalized diagrams for basalts (**a**) and intermediate/felsic (**b**). Primitive mantle-normalized multi-element diagrams for basalts (**c**) and intermediate/felsic (**d**). The data of OIB along with normalization values of both primitive mantle and chondrite are from Sun and McDonough (1989)

lower Sr contents (52–499 ppm) as compared to the basaltic rocks (Zr = 15–369 ppm, Nb = 44–81 ppm, Y = 11–39 ppm, Rb = 2–39 ppm, Ba = 4–798 ppm, Ta = 3–5 ppm, Th = 4–6 ppm, U = 1–2 ppm, Sr = 127–776 ppm). Compared with trachyandesites/trachytes, the felsic rocks show low contents of LILE and HFSE. The total REE contents increase from the basaltic (180–207 ppm) through the trachyandesitic/trachytic (671–710 ppm) to the felsic rocks (711–728 ppm).

In chondrite-normalized REE plots (Fig. 8a, b), the LREE enrichment and HREE depletion characterize the NV ($(La/Yb)_N$ = 10–23; $(Tb/Lu)_N$ = 2.29–4.23; $(Nb/Yb)_N$ = 16–33; $(Gd/Yb)_N$ = 2.3–2.9), similar to the ocean island basalts (OIB, Sun and McDonough, 1989). The ratios of LREE/HREE increase from basalts ($(La/Yb)_N$ = 10–15) to trachyandesites/trachytes and rhyolites ($(La/Yb)_N$ = 10–21) with moderately low concentration of HREE ($(Ho/Yb)_N$ = 1.06–1.14), displaying strong fractionation between LREE and HREE. The basalts fall within the field array of Nb-rich basalts (Fig. 7b). The high concentrations of both Zr/Hf (43) and La/Nb (0.95) ratios in the basalts reflect their origins from mantle-derived OIB (Taylor and McLennan, 1985). The OIB and the studied basalts show close similarities in Nb/Ta, Nb/U, and Ce/Pb ratios (17.5, 47, and 25 ± 5 vs. 17, 34, and 38, respectively) further reinforcing mantle source for the NV. The most differentiated trachyandesites/trachytes show higher contents of both LREEs and HREEs than the basalts ($(La/Yb)_N$ = 19–23 vs. 15–17, respectively) (Fig. 8a, b). They show weak negative Eu anomalies (Eu/Eu* = 0.36–0.84, Fig. 8b) compared to those in basalts (1.16–1.21, Fig. 8a), suggesting that a plagioclase is lacking in the magma source of the basalts, and so, their REE array displays no negative Eu troughs. In mantle-normalized trace element diagrams (Fig. 8c, d, Sun and McDonough (1989), the lava specimens show high enrichment degree for HFSEs (such as Nb, Ta, Zr, and Hf), LILEs, and LREEs with noticeable Pb, Sr, P, and Ti troughs especially in trachyandesites and trachytes (Fig. 8d). Moreover, the trachyandesite/trachyte and rhyolite specimens have higher concentrations of Th, U, Ta, and Hf than the basaltic rocks, demonstrating their high degree of fractionation.

Composition of primary magmas

The common occurrence of olivine and pyroxene phenocrysts in basalts of the NV and the equilibrium of Fo_{77-65} with their host liquids (Mg#55) of olivine crystals are not demonstrative of a primitive magma. In order to remove the fractionation influence and achieve the initial melt composition benchmarks (Mg# = 68–72, 300–500 ppm Ni, 750 ppm Cr; e.g. Green and Falloon 2005), we should add the appropriate fractionated crystal phases into the quantified compositions. Olivine represents the prevailing phenocryst phase in basalts, demonstrating olivine-controlled fractional crystallization. The least-evolved basaltic sample (N_2) was assumed as the parent magma for the whole NV. The N_2 magma is not compatible with the primary magma that should occur in balance with the mantle because it contains low MgO content (5.34 wt%), as the results of olivine and clinopyroxene fractionation from initial source. In the N_2 melt, the Fo content varies from 77 (core) to 60 (rim). For the melt, a balance $(Fe^{2+}/Mg)\ Kd_{ol}$ of 0.3 (Roeder and Emslie 1970) and an $Fe^{3+}/\Sigma Fe$ ratio of 0.23 was presumed, according to the $Fe^{3+}/\Sigma Fe$ ratios and water content that were calculated by Kelley and Cottrell (2009). The effect of crustal assimilation is neglected in NV based on isotopic data proposed by Abu El-Rus (2016). The positive Eu array characterizing the mafic rocks (Eu* = 1.05, Fig. 8a) discloses irrelevant separation of plagioclase during fractionation in the formation of their magma. So, the olivine is the only fractionated phase in adjusting the composition of the primary magma. We have used the Petrolog model version 3.1.1.3 (http://petrolog.web.ru/latest.html, Danyushevsky and Plechov, 2011) to define an initial magma composition for N_2 melt. This model requires an addition of olivine until a magma composition in balance with the mantle is achieved. The MnO (0.3 wt%) and CaO (0.2 wt%) contents should be constant of the olivines, and the SiO_2, FeO, and MgO concentrations were calculated as a utility of the content of Fo using 0.3 and 0.23 values for $(Fe^{2+}/Mg)\ Kd_{ol}$ and $Fe^{3+}/\Sigma Fe$ ratios, respectively, for the melt. This model shows that c. 15–20% olivine requests to be added to attain the balance with mantle olivine composition (Fo_{89-90}, Mg# = 73, Mg > 9, K_D (Fe+Mg) = 0.29). The estimated SiO_2, FeO, MgO, CaO, Na_2O, K_2O, and H_2O contents of the initial magma are 47.2 wt%, 7.73, 11.8 wt%, 10.9, 2.98, 0.13, and 3.1 ± 0.9 wt%, respectively. The calculated temperatures (considering specimens with MgO >9 wt%, Fe^{3+}/Fet = 0.1, and olivine Fo_{89-90}) range from 1359 to 1377 °C, by using the equations of Wood (2004) and Putirka's model (2008). Melting pressures vary from 1.6 to 1.77 GPa for the primary magma which corresponds to a mantle source at 16.7–18.7 kb in the temperature ranging from 900 to 1100 °C, near the garnet–spinel peridotite transition boundary (O'Neill 1981), matching with the pressure estimation (11.7–19.4 kb) determined by the clinopyroxene geobarometer (Nimis 1999). Eskandari (2016) concluded that the depth of magma formation was proposed between 27 and 35 kbar, matching to the deep mantle melting along the lithosphere-asthenosphere boundary melting for the alkaline magmas.

Discussion

Petrogenesis

Genetic characters of the Natash volcanoes

The ratios of incompatible elements (like La/Yb, Nb/La, Zr/Nb, Nb/Th, Th/Yb, and Nb/Yb) can be used as indicators to trace their mantle source because the processes of partial melting and crystal fractionation have no effect on the behaviour of these ratios (Weaver, 1991). The rock samples of the NV are plotted in OIB field with a HIMU signature based on comparatively high Nb/La (1–2), Th/Y, and Nb/U along with low La/Yb (<50, Fig. 9a, b). The high Nb/Th (10–18) and La/Yb (10–22) ratios along with low Zr/Nb ratios (5–8) of the NV are plotted near OIB source (Fig. 9c, d). The basaltic specimens show much higher Nb (38–84 ppm), Zr (222–369 ppm), and ΣLREE (180−207 ppm) than E-MORB (Nb = 8.3 ppm, Zr = 73 ppm, ΣLREE = 32.35 ppm) and analogous with OIB (Nb = 48 ppm, Zr = 280 ppm, ΣLREE = 165 ppm, Sun and McDonough, 1989). Moreover, NV are categorized by moderately high ratios of Nb/Ta (17–19) which are akin to those of the OIB (15.9; Pfänder et al. 2007) and chondrite (19.9; Münker et al. 2003). In addition, all the NV display moderately high ratios of Zr/Hf (36–67) and Th/Nb (0.06–0.10) which are close to the mantle-derived magma (Zr/Hf = 17.535–45 and Th/Nb = 0.117; Hofmann, 2003) compared with those ratios of continental crust (Nb/U ~ 9, Zr/Hf < 30, Th/Nb = 0.44, Rudnick and Gao, 2003). These geochemical features reflect a fertilized OIB-type mantle source for the NV. Based on Sr-Nd-Pb-Hf isotopic ratios, the NV were chiefly resulted from the HIMU, EMI, and depleted mantle (DM) endmembers, with a large amount of HIMU type (Abu El Rus et al., 2018) as has been previously concluded by Khalaf et al. (2018).

The intermediate and felsic volcanoes in Wadi Natash show high contents of Ga/Al ratio (4–15), HFSEs plus Ce (563–1123 ppm), and REEs (303–564 ppm), representative of A-type granite characters (Fig. 10a–c, Whalen et al. 1987; Eby, 1990). Eby (1990) used the Y/Nb ratio as an imperative key with a value of 1.2 in differentiating between A_1- and A_2-type granites. A_1-type granites

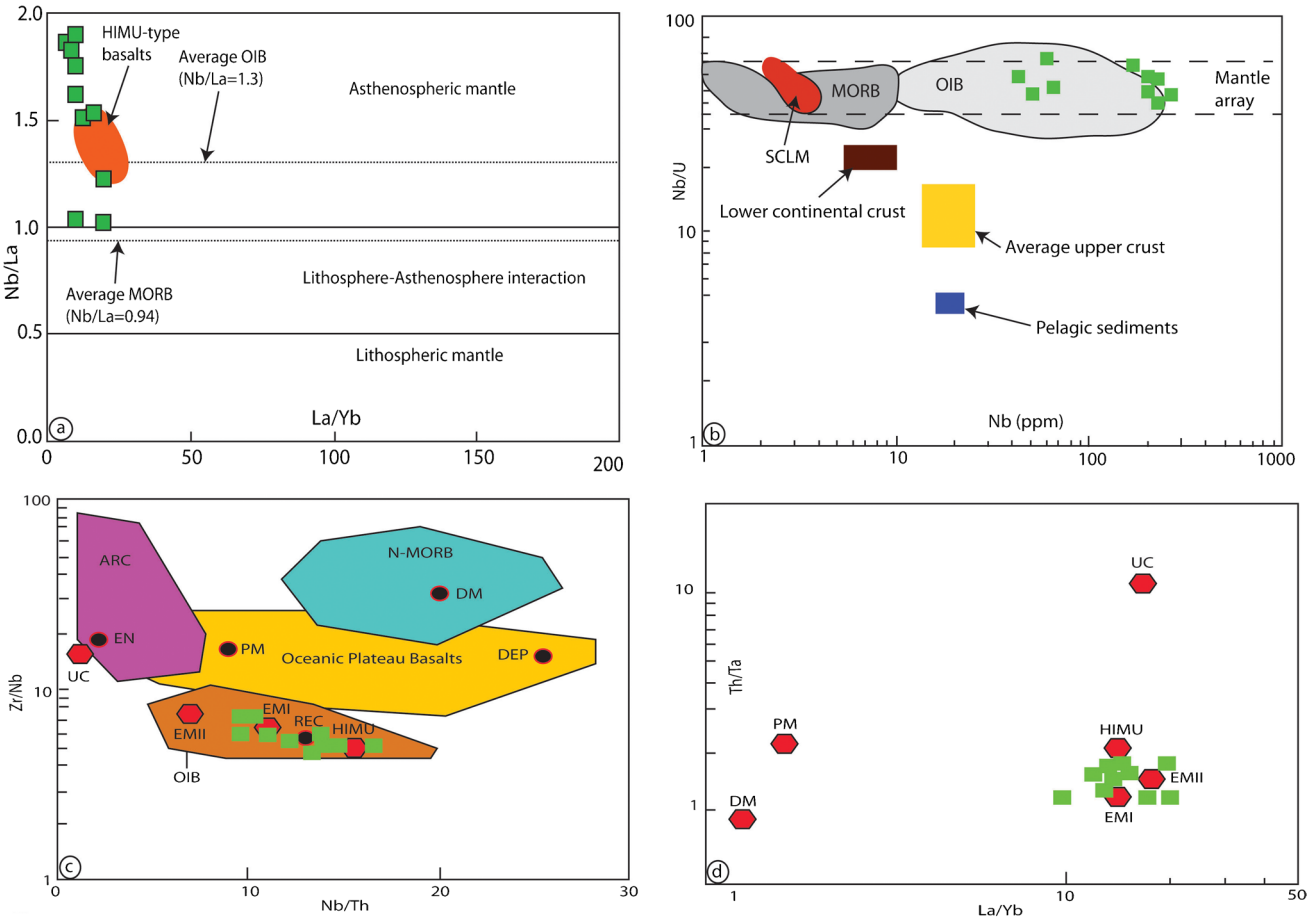

Fig. 9 Geochemical characters of the Natash volcanoes. **a** La/Yb vs. Nb/La variation in the studied Natash volcanoes showing their affinity to the HIMU-type basalts (Willbold and Stracke 2006). Average Nb/La values for MORB and OIB are from Sun and McDonough (1989), respectively. **b** Nb/U vs. Nb (ppm). **c** Zr/Nb vs. Nb/Th diagram (after Pearce 2008). **d** Th/Ta vs. La/Yb diagram. The shaded field represents the range of MORB, subcontinental lithospheric mantle (SCLM) and oceanic island basalts (Ce/Pb = 25 ± 5; Nb/U = 47 ± 10; Hofmann 2003). The average value of continental crust (Rudnick and Gao 2003) is also included for comparison. MORB, mid-ocean ridge basalt; N-MORB, normal mid-ocean ridge basalt; E-MORB, enriched mid-ocean ridge basalt; OIB, ocean-island basalt; DM, depleted mantle; HIMU, high μ mantle; EMI, enriched mantle I; EMII, enriched mantle II; UC, upper continental crust; REC, recycled component; En, enriched component; DEP, deep depleted mantle

were resulted from OIB sources by fractional crystallization in an intraplate or rift settings, while A_2-type granites were formed from subcontinental lithosphere or lower crust magmas in post-orogenic settings (Eby 1992). The NV have low Y/Nb ratio ranging from 0.3 to 0.8, similar to the A_1-type granites (Y/Nb < 1, Fig. 10d). A_1-type granite affinity for these volcanoes is confirmed by high Nb concentration relative to Y and Ce contents (Fig. 10e). Furthermore, the NV have high Nb* and Ta* values that are similar to the distinctive OIB-derived A_1-type rhyolites (Fig. 10f, Fan et al. 2021). A-type granites universally need an expressively high temperature, reflecting mantle-derived magmas in their genesis (King et al. 1997). Abu El-Rus et al. (2018) determined the zircon saturation temperatures (ZSTs) for the NV, which range from 830 to 930 °C for trachytes and ~900 °C for rhyolites that are recorded in A-type granites (>830 °C; Miller et al., 2003).

Magmatic evolution of the Natash volcanoes

The studied NV show a wide compositional discrepancy (e.g. SiO_2 = 45–72 wt%; Table 1), proposing that their parent magma–derived melts were affected by different degrees of fractional crystallization (FC, Fig. 11). The proofs of the FC are supported by the following: (1) the felsic rocks are scarce as compared with the basalts that are reliable with a small quantity of magmas formed by FC (Shao et al., 2015) and (2) the NV delineate linear trends on major/trace elements vs. Zr as differentiation index, which are reliable with the trends of FC (Fig. 11). The wide range in La contents (40–150 ppm) and restricted variation of La/

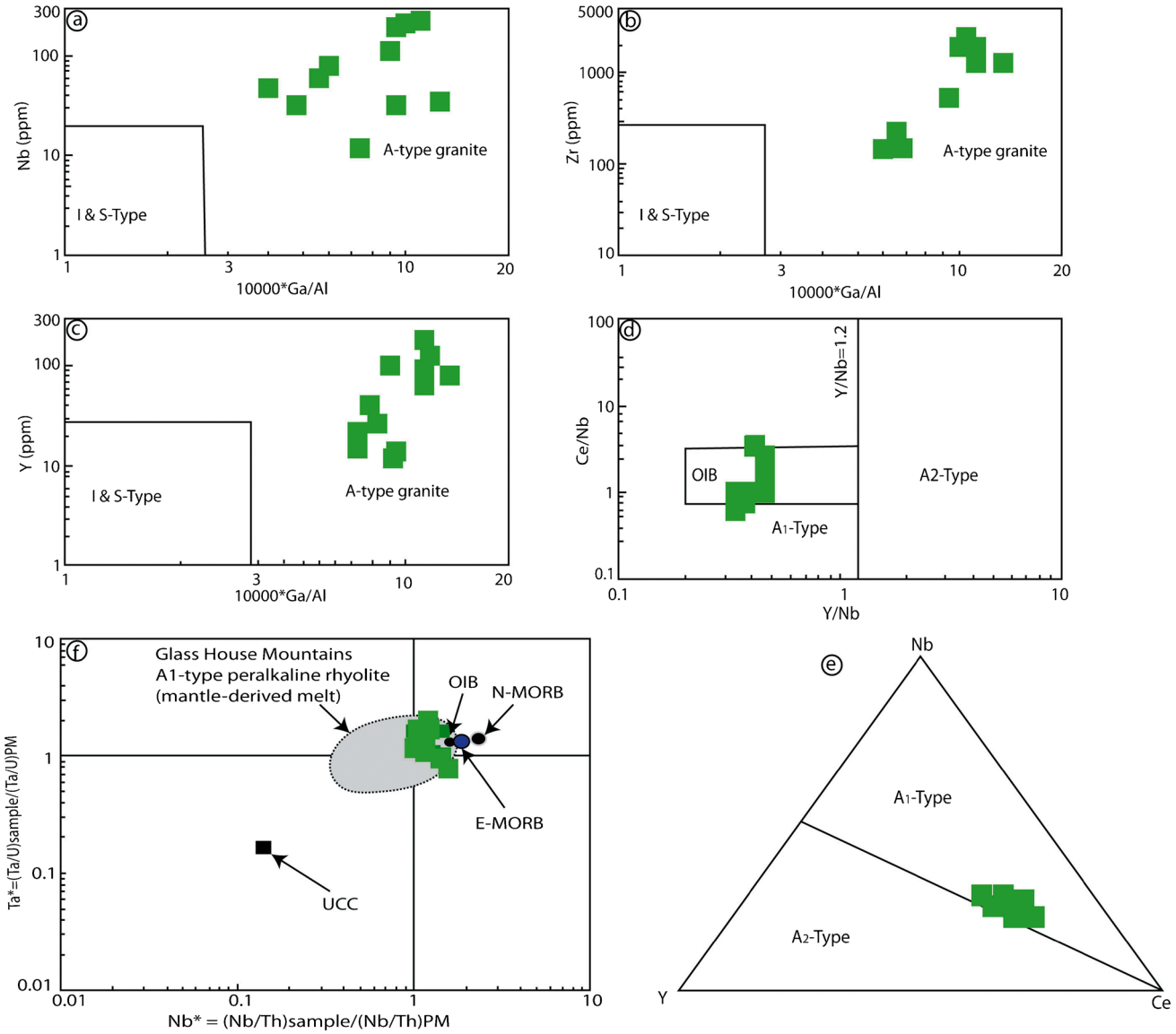

Fig. 10 A-type characters for the Natash volcanoes. Ga/Al ratio vs. Nb (**a**), Zr (**b**), and Y (**c**). The chemical discrimination diagrams after Whalen et al. (1987) and Eby (1992). **d** Y/Nb vs. Ce/Nb for discriminating between A_1- and A_2-type granite. **e** Nb-Y-Ce ternary diagram for discriminating between A_1- and A_2-type granite. **f** Ta* vs. Nb* diagram of the Natash volcanoes (after Niu and Batiza 1997; $Ta^* = [Ta/U]_{sample}/[Ta/U]_{PM}$; $Nb^* = [Nb/Th]_{sample}/[Nb/Th]_{PM}$). The distinctively high Nb* and Ta* of A-type alkaline volcanics are inherited from their parental melts with high Nb and Ta. The A_1-type Glass House Mountains rhyolite are from Shao et al. (2015)

Sm ratio (4–6) together with high Yb contents recorded in high differentiated rocks (9–13 ppm) are further supported for FC (Fig. 7d). The compatible elements like Cr, Co, V, and Sr decrease, while the incompatible elements, such as LILE (like Rb), HFSE (Nb, Ta, Y), and REE, increase from basalts to trachyandesites/trachytes and rhyolites with increasing Zr as abscissa (Fig. 11), signifying a continuous comagmatic evolutionary trend. The decrease of Fe, MgO, and CaO contents joined with Ni and Cr refers to the olivine, clinopyroxene, and spinel fractionation. The decreasing concentration of Eu, Ba, and Sr in the trachyandesites/trachytes-rhyolites, relative to basalts, designates that their magma underwent fractionation of plagioclase. Furthermore, the low content of Ti presented by these rocks reveals fractionation of amphiboles and/or Fe-Ti oxides. The decrease of TiO_2, Fe_t, P_2O_5, and SiO_2 contents with increasing fractionation index conforms with the fractionation of titanite, magnetite, and apatite. The trachyandesites/trachytes and rhyolites show high contents of both La/Gd (4.5–6.5) and Lu/Gd (0.03–0.1) ratios along with negative MREE anomaly (Fig. 8), demonstrating a significant participation of amphibole fractionation from the melt because

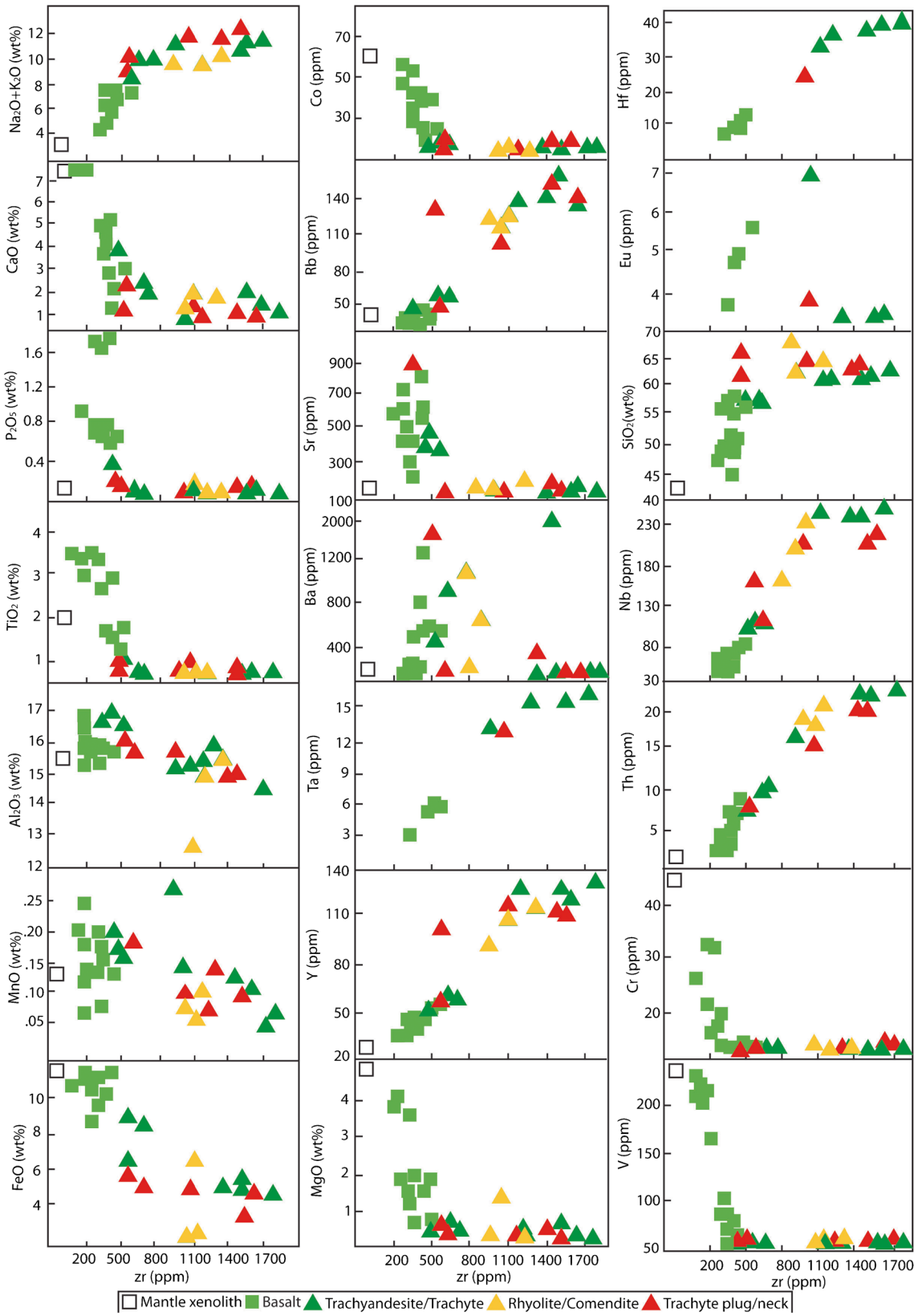

Fig. 11 Harker variation diagrams showing Zr used as differentiation index vs. major/trace elements for the Natash volcanoes

the amphibole fractionation causes a decrease in MREE and HREE (chiefly MREE) (Chung et al., 2003).

The high enrichment of Nb, Ta, and Ce contents as well as high Nb/Y ratio (1.3 to 1.88 compared to ~0.4 in continental crust) in the studied NV (Table 1) reflects the absence of any crustal involvements during the arising melt (Rudnick and Gao, 2003). The high Nb/U and Ce/Pb ratios characterizing the NV (34–68 and 28–81, respectively) signify mantle-derived OIB (e.g. Nb/U = 47, Ce/Pb = 25 ± 5 in OIB (Hofmann, 2003), compared to those ratios in the continental crust (9–5, respectively, Rudnick and Gao, 2003)). In the La/Yb vs. Nb/La, Nb/U vs. Nb, and Th/Ta vs. La/Yb plots (Fig. 9), the NV samples supplementarily strengthen its affinities to OIBs with the lacking influences of crustal contamination. The NV are characterized by Nb and Ta enrichment which further support the insignificant contribution of crustal constituents, because the crustal contamination decreases Nb and Ta concentrations and increases the ratios of Th/Ta and Th/Yb during the magma evolution (Niu and O'Hara, 2003). The presented radiogenic data designate that the NV are categorized by their elevated $^{143}Nd/^{144}Nd$ (0.512653–0.512761) and low $^{87}Sr/^{86}Sr$ isotopic ratios (0.7030–0.70286, Abu El Rus et al., 2018), which may confirm that the NV sequences were evolved from OIB-like mafic magmas via fractional crystallization without crustal contamination. The high enrichment in both LILEs and HFSEs as well as isotope ratios characterized the NV, analogous to other alkaline ring complexes from SED ($^{143}Nd/^{144}Nd > 0.51270$ and $^{87}Sr/^{86}Sr = 0.7030–0.7050$, Landoll et al. 1994), which are reliable with the mantle-derived magmas for the alkaline rocks (Mogahed, 2016). In conclusion, we suggest that the alkali volcanoes in the Wadi Natash were originated from an OIB-derived mantle source and prolonged fractional crystallization with negligible crustal contamination subscribed to the compositional variations from mafic to felsic rocks.

Mantle metasomatism accompanying Nb mineralization

Natash volcanoes are categorized by LREE enhancement and HREE reduction (Avg. $(La/Yb)_N = 9$; $(Dy/Yb)_N > 2$; $Sm/Yb)_N > 1$)) that are reliable with a garnet-bearing HIMU-OIB-type source (Wang et al., 2009) as the HREE, denoted by Yb, have high partition coefficients to garnet ($Kd_{Ybgarnet} = 5.5$ at 3.0 GPa; Salters and Stracke, 2004). The degree of partial melting of mantle source can be evaluated by the degree of HFSE and LREE enrichment (Fan et al., 2021). The data of the NV display that their source may suffer partial melting via low degree (<5%) in the $(Sm/Yb)_N$ vs. $(La/Sm)_N$ plot (Fig. 12a). The basalts are linked to Nb-rich basalts (Fig. 7b). Two chief assumptions have been proposed for the origin of Nb-rich basalts: (1) composite mingling of OIB and MORB magmas (model 1, Hastie et al., 2015) or (2) partial melting of mantle that has been affected by subducted slab melts via metasomatism (model 2, Hastie et al., 2011). Any igneous rocks which were formed by magma mingling have a comprehensive array of Nd isotope (Yang et al., 2006); however, the uniform values of the $^{143}Nd/^{144}Nd$ (0.512653–0.512761, Abu El Rus et al., 2018) do not support the magma mixing in the mantle source for the NV. Model 2 proposes that the Nb-rich basalts are related to Nb-rich minerals of the mantle source, which are created by mantle metasomatism (Hastie et al., 2011). If partial melting of the Nb-poor minerals involved in the mantle source happens, the Nb/La ratios show no variation with discrepancies in the degree of partial melting as shown by La/Yb ratios because of comparable distribution coefficients for Nb and La in the mantle (Sajona et al., 1996). The NV samples show an inverse relationship between the ratios of Nb/La and La/Yb (Fig. 12c), signifying the existence of the Nb-rich minerals in the mantle source that was formed by model 2.

The OIB-like source becomes enriched source when Nb-REE-rich melts intermingle with depleted mantle via mantle metasomatism (Pilet et al., 2011). Many processes have been involved for the extremely enriched geochemical features of OIB like recycled oceanic crust, terrigenous sediments, mantle plume, or asthenosphere-derived melts (Raghuvanshi et al. 2019). The Natash volcanoes show high La/Sm ratio (4–6) which argue against the involvement of old subducted oceanic crusts (La/Sm <1) to be source materials for the NV and overall OIB-related constituents (La/Sm >1, Niu and O'Hara, 2003). Moreover, terrigenous sediments are categorized by Pb enhancement and poor contents of HFSE and REE (Niu et al., 2011), opposing the geochemical features of the NV. The enrichment of LREEs and HFSEs (Fig. 8), joined with high ratios of Nb/La (1.1–1.87) and Nb/U (38–68) as well as low Th/Zr ratios (0.01–0.02) and depletion of Nd isotopic ratios (0.512653–0.512761, Abu El Rus et al. 2018), denotes metasomatized lithospheric mantle triggered by asthenosphere-derived melts as reasonable model (Sahoo et al. 2020). The melt-related metasomatism and fluid-related metasomatism are responsible for the metasomatic lithosphere mantle for NV (Fig. 12d). Such type of metasomatism is common in lithosphere mantle in the ANS that was attributed to fluid released during subduction in Neoproterozoic Era (Shaw et al. 2007) or rising plume through Phanerozoic Era (Rooney et al., 2014).

In a rift regime, outpouring of the asthenosphere can offer a conduit for degassing of Earth (Martin, 2006; Huang et al., 2014), where HFSE-REE-rich melts along with alkali components ascend from the asthenosphere to the lithospheric mantle (Pilet et al., 2008). Such enriched melts interact with the depleted lithospheric mantle as hydrous metasomatic veins composed of amphibole and phlogopite (Pilet et al. 2011; Zhang et al. 2020). The melting of such amphibole-rich metasomatic veins can yield melts with comparable

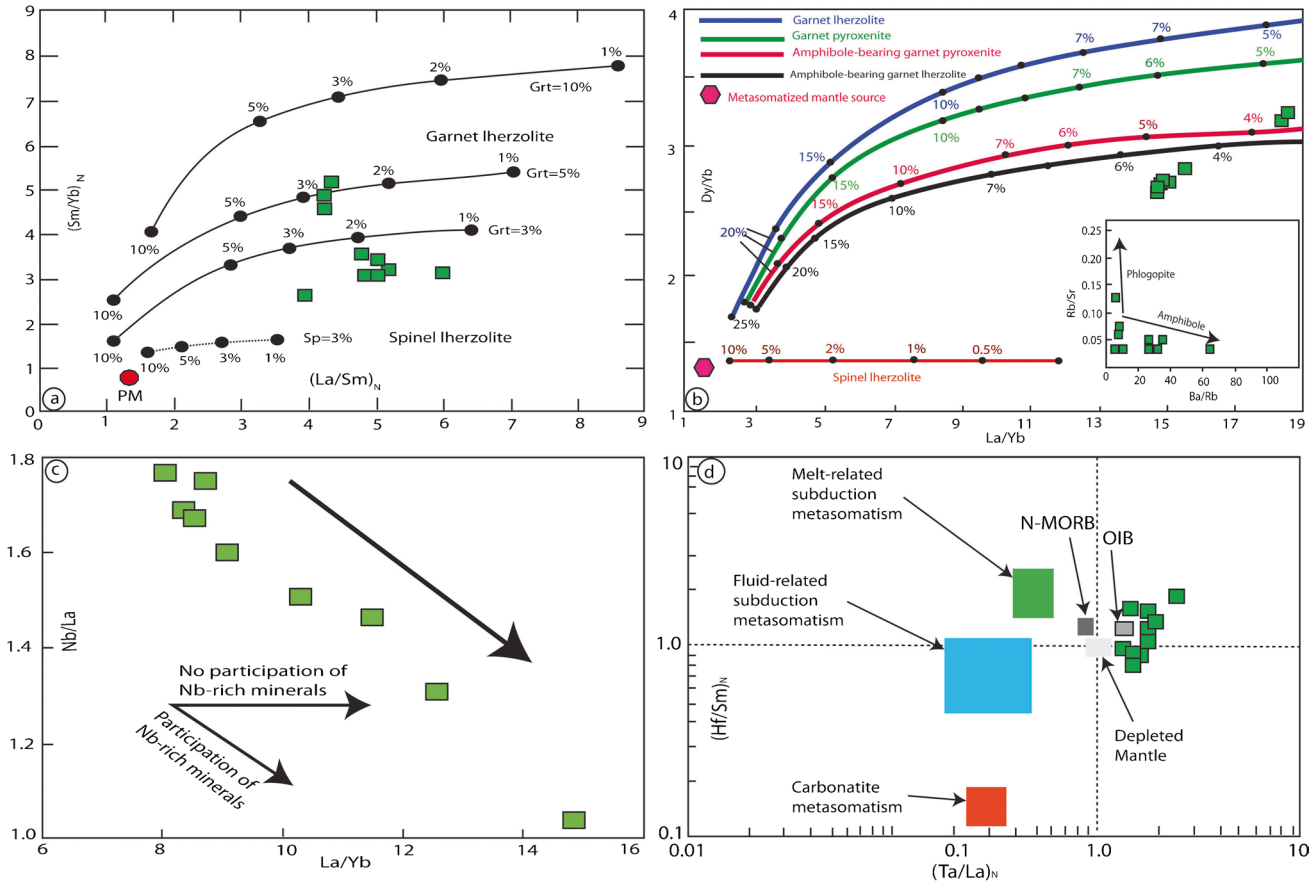

Fig. 12 Petrogenetic characters of the Natash volcanoes. **a** $(Sm/Yb)_N$ vs. $(La/Sm)_N$ trace element binary plot (modified from Li et al. 2019). Batch melting trends depending on the non-modal batch melting equations of Shaw (1970). Melt curves are drawn for spinel-lherzolite (with mode and melt mode of ol53% opx27% cpx17% sp3% and ol6% opx28% cpx67% sp11%; respectively; Kinzler 1997) and for garnet-lherzolite (with mode and melt mode of ol60% opx20% cpx10% gt10% and ol3% opx16% cpx88% gt9%; respectively). The composition of the primitive lherzolitic mantle is plotted (according to Sun and McDonough 1989). Partition coefficients for plots **a** and **b** are from McKenzie and O'Nions (1995). **b** La/Yb vs. Dy/Yb ratio showing the fractionation-corrected melts of alkaline Natash volcanoes compared to the non-modal fractional melting trajectories of an amphibole garnet lherzolite (8% modal abundance of amphibole), garnet lherzolite, garnet pyroxenite, and spinel lherzolite (melting trajectories are from McCoy-West et al. 2010). **c** Nb/La versus La/Yb (Sajona et al. 1996). **d** $(Hf/Sm)_N$ vs. $(Ta/La)_N$ (La Flèche et al. 1998) diagram

geochemical features of alkaline magmas as has evidenced experimentally by Pilet et al. (2008). The low K_2O contents characterized the basaltic rocks (1991–14,604 ppm, Table 1) that strengthen the existence of K-rich hydrous phases (e.g. amphibole or phlogopite) in the mantle source, which are comparable to melts created by partial melting of an amphibole-bearing peridotite (K < 20,000 ppm, Späth et al., 2001. The mafic lavas from NV have low Rb/Sr (<0.1) and high Ba/Rb (>20) ratios (Fig. 12b, inset), proposing the occurrence of amphibole rather than phlogopite in magma source (Furman and Graham, 1999). In the Dy/Yb vs. La/Yb melting model (Fig. 12b), the parent magma of the NV was formed from an amphibole-bearing garnet lherzolite via less than 5% degree of partial melting, compatible with its pervasive existence in the lithospheric mantle of Arabian-Nubian Shield (ANS, Weinstein et al. 2006). Therefore, the basalts in the Wadi Natash possibly created from an enriched lithospheric mantle via metasomatism subscribed to the HFSE-REE-rich source.

Mechanisms of Nb enrichment in the Natash volcanoes

Previous studies have proposed that long history of fractional crystallization and hydrothermal metasomatism in combination with partial melting are responsible for the REE and HFSE enhancement in alkaline rocks (Huang et al., 2014; Xiang et al., 2017). The NV are enriched in Nb (80–283 ppm) compared to other ring complexes in SED like El Kahfa ring complex (Nb = 36–226 ppm, Hegazy et al., 2016), revealing mineralization potential for Nb deposit. The differentiation paths from basalts to trachytes/rhyolites

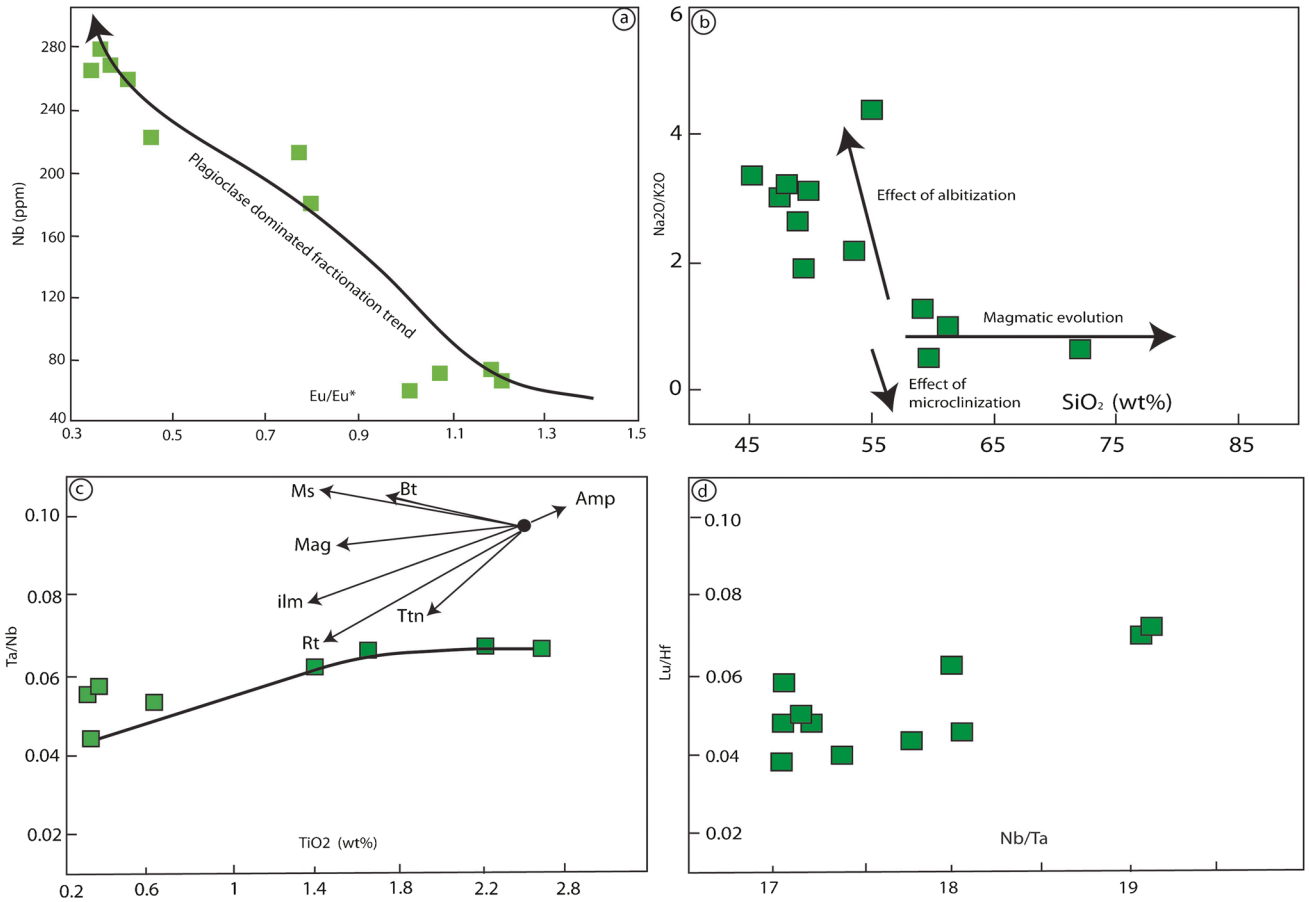

Fig. 13 Diagrams involving various processes responsible for Nb enrichment. **a** Nb vs. Eu/Eu* presenting an increase of Nb content as the result of Nb-poor plagioclase fractionation. **b** Na_2O/K_2O ratio vs. SiO_2 displaying the dominant albitization process during the evolution of NV. **c** Ta/Nb vs. TiO_2 (after Stepanov et al. 2014) showing increasing of Ta/Nb ratio in residual melt. **d** Nb/Ta vs. Lu/Hf binary diagram

(Fig. 11) are accompanied by an increase of Nb content in the remaining melts as has been documented by Zhu et al. (2020) and Wang et al. (2021). The inverse relation between the whole-rock Eu/Eu* vs. Nb proposes that the increase of Nb concentrations is well matched with continuous elimination of plagioclase during magma evolution (Fig. 13a). These explanations designate that fractionation processes play an important role in raising the Nb contents during the volcanic evolutions, in which fractionation of Nb-poor feldspars leads to the steady Nb enrichment in the residual melt as crystallization proceeds (Zhu et al., 2020) as has been observed in Late Triassic A_1-type alkaline volcanoes, East Kunlun Orogen, China (Zhu et al., 2022). Post-magmatic alteration and hydrothermal metasomatism may increase Nb contents, although Nb concentrations are generally enhanced by magmatic processes (Estrade et al., 2014). Some researchers propose that the processes of hydrothermal alteration play a significant role in the enhancement of Nb, REE, and additional rare metal mineralizations (Ballouard et al., 2016), which can produce compounds with ligands (e.g. F^-, Cl^-) and assist their mobilization and concentration (Timofeev et al., 2015; Girei et al., 2019). In the present study, the NV display various features of hydrothermal alteration like the presence of the interstitial biotite flakes along feldspar borders (Fig. $3z_1$), typical characteristics of hydrothermal biotitization. In addition, most of the rock specimens have high Na/K ratios (up to 5), signifying the presence of sodic metasomatism (albitization) that affects the NV (Fig. 13b).

The petrographic observations show the presence of accessory titanite, apatite, zircon, sphene, and ilmenite associated with phenocrysts (Fig. 3). Many authors described and analysed the titanite crystals that are enriched in Nb_2O_5 (Nb_2O_5 = 0.5–3.3 and 1.1–3.3 wt% in magmatic and hydrothermal metasomatic crystals, respectively) in Fangcheng alkaline rocks, East Qinling (Zhu et al. 2020, 2022), China. They concluded that the Fangcheng's parent magma was enriched in Nb as the result of the occurrence of an enriched mantle formed by low melting degree. The TiO_2 contents increase (from 0.2 to 2.8 wt%) with an increasing Ta/Nb ratios (from 0.04 to

0.06, Fig. 13c), signifying a conceivable role of titanite for presentation the Nb/Ta ratios in partial melts, as has been formerly determined for titanite grains in alkaline rocks (Zhu et al., 2020). Furthermore, ilmenite grains observed in the NV (Fig. 4a) may consider as source of Nb and Ta because ilmenite usually has high contents of Nb and Ta recorded in intermediate-felsic magma. Nb concentrations are commonly enhanced by magmatic processes, although hydrothermal metasomatism may be universally responsible for Nb mineralization (Estrade et al., 2014). The low Zr/Nb (3.5–6.5) along with the positive correlation between Nb/Ta (16–19) and Lu/Hf (0.04–0.06) observed in the Natash lavas (Fig. 13d) deliver supplementary proof that their mantle source was affected by metasomatized fluids that led to the Nb enrichment observed in the subaerial basalts (e.g. Pfänder et al., 2007). The inverse relationship between Nb/La and La/Yb ratios (Fig. 12c) further supports the occurrence of the Nb-rich minerals in the mantle source that was formed by mantle metasomatism. So, it is concluded that Nb enhancement of the NV is resulted from Nb-rich accessory minerals like titanite/ilmenite crystals inherited from mantle-derived OIB-type parental magma (magmatic processes), fractionation of Nb-poor feldspar, and post-magmatic hydrothermal phenomena that played a role in HFSE remobilization to form Nb-rich minerals as has been proved by Zhu et al. (2020, 2022).

The nature of Natash plumbing system

Many magma chambers situated at different depths have been recognized underneath intraplate alkaline volcanoes that usually generate from deep mantle and pass over thick

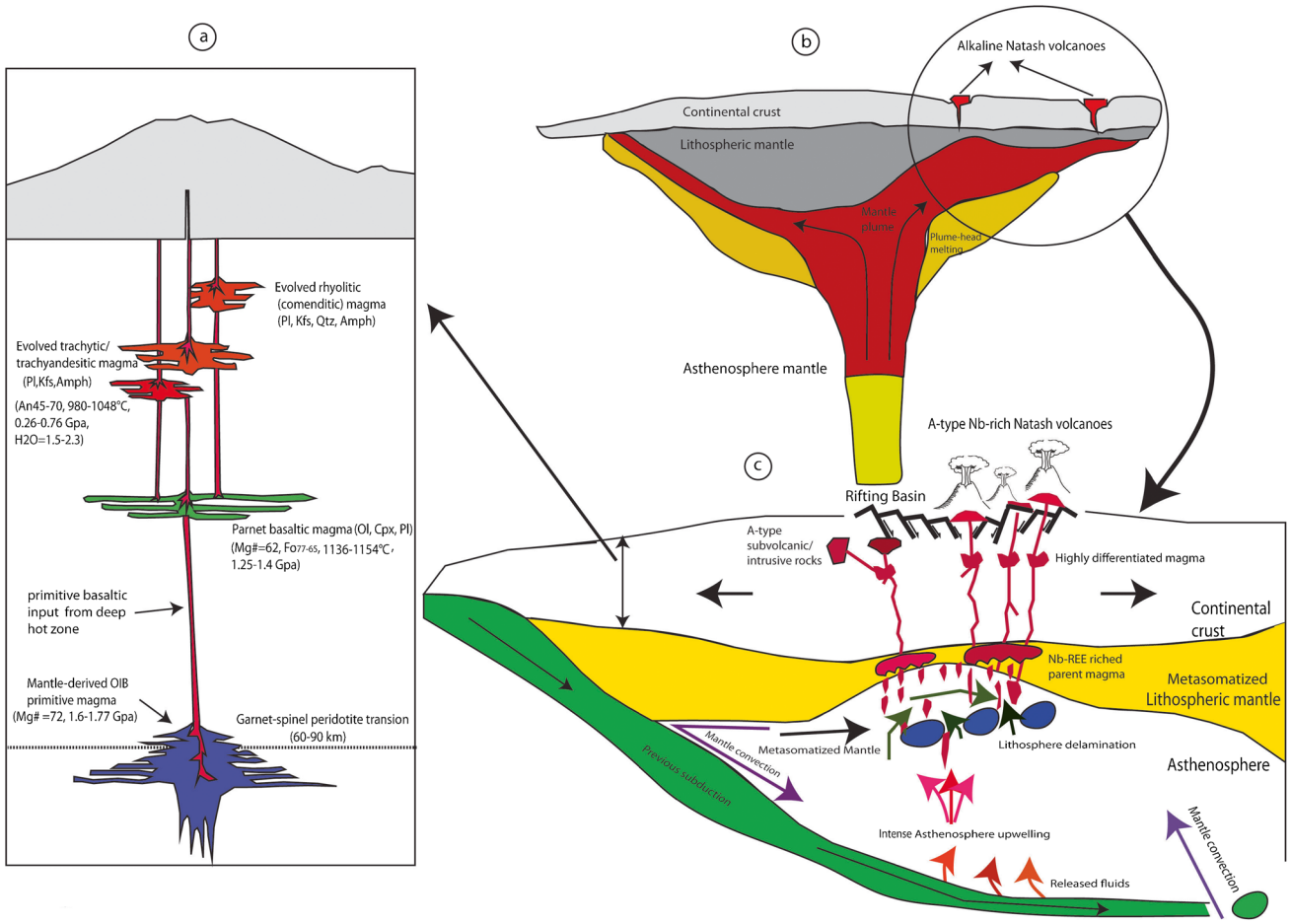

Fig. 14 Schematic illustration for the Late Cretaceous alkaline magmatism in the Natash area. **a** Cartoon model of the magma plumbing system beneath Natash volcanoes based on geobarometric calculations. **b** A not to scale cartoon (modified after Sen and Chandrasekharan 2011) depicting the plume-induced thinning of the lithosphere that melted at the rift zones to generate alkaline magmatism including Natash volcanoes. **c** Partial melting of a metasomatized mantle triggered via crustal extension and lithospheric thinning, resulting in the formation of Nb-REE-enriched parent basaltic magma that evolved to mafic-intermediate-felsic magmas (modified after Wu et al. 2023). The asthenospheric upwelling via diapiric mantle and delamination melting prompted by lithospheric thinning into the convecting mantle following ancient subducted-related fluid metasomatism during Pan-African Orogeny has been proposed to create the Natash parent melts along fault-controlled extensional tectonics

crustal successions towards shallower crustal levels (Marzoli et al., 2015). Petrological and geochemical studies reveal that NV display multi-eruptions involving basalts, trachytes, trachyandesites, rhyolites, or comendites (Fig. 7a) that occurred within the Earth's crust (Fig. 14a). The parent magma was created by low degree of metasomatized amphibole-bearing garnet mantle source under high pressure at 1.6–1.77 GPa (>50 km, mantle-crust boundary) similar to the formation of alkaline basaltic melts derived from hydrous phase-rich peridotites at ca. 2.0–2.2 GPa and 1200–1300 °C (Green and Falloon 1998). The Natash parent magma underwent initial fractionation of olivine and clinopyroxene followed by fractional crystallization of plagioclase and amphibole together with apatite and Fe-Ti oxides in more evolved magmas. Thermobarometric outputs give proofs that the NV were evolved through the polybaric fractional crystallization (Fig. 5f). For example, fractionated olivine crystals (Fo_{77-65}) suggest stagnation deep zones at 1.4–1.25 GPa (14–12 kbar or 50–43 km), while plagioclase phenocrysts (An_{70-45}) reflect shallow crustal levels at 0.76–0.26 GPa (7–2 kbar or 26–9 km) accompanying by H_2O contents (from 2.5% to 1.5 w% for high to low An), signifying magmatic injections from deep to shallow H_2O degassing (Firth et al., 2014; Aiuppa et al., 2019). The shallow depth is reinforced by amphibole occurrence in some evolved trachyandesites and trachytes (Fig. 3s) in which the high melt H_2O content (≥4 wt%) at mid-shallow depth (~2 kbar) is crucial to stabilize amphibole on intermediate melt compositions (Pontesilli et al. 2022).

The existence of various phenocryst assemblages (particularly feldspar) and their disequilibrium textures in the NV (Fig. 3) propose also that their feeding magma encountered diverse stagnation regions at dissimilar levels of nucleation or dissolution surfaces during rise to the surface. Phenocryst disequilibrium textures like zoning, opacite/reaction rims, and corrosion/resorption designate variations in the magmatic circumstance such as drops of water content, degassing phenomena, and magma dehydration because of pressure and temperature change during magma ascent, or the mixing of compositionally and thermally discrete magmas under open system (Holnes et al., 2019). This is reinforced by the existence of sieve textures in the plagioclase feldspar (Fig. 3g, m–o), which can be interpreted either by compositional variations in magma, magma mixing, or fast decompression of plagioclases to melts where quick ascent of magma may maintain liquid inclusions as glass pockets (e.g. Renjith 2014). The rapakivi and antirapakivi textures observed in feldspar (Fig. 3r) are inferred as the products of magma mixing or convection self-mixing as the result of discrepancies in temperature with no addition of new magma (i.e. recharge). The oscillatory zonation observed in plagioclase (Fig. 3k, l, and z_2) is the reply of inconsistent external circumstances because of limited convection of the crystal-derived magmas (Renjith 2014). NV involve highly evolved Hawaiian-Vulcanian crystalline eruptive products (dominant plagioclase) with no mark of primary magma in which crystal-rich lavas require extended residence periods with the prolonged relaxation pause through which volatile flux and melt additions that control eruption frequency and crystal content lead to the complex textures in plagioclase crystals (e.g. McCarthy et al., 2020). So, we infer that the plumbing system of the NV can be interpreted as high crystalline evolved magma mushes (crystal-rich lavas) stagnated and fractionated at dissimilar depths during magmatic evolution preceding to eruption as the result of low volatiles, magma fluxing, and magma frequency with complete absence of primitive mafic rocks (see Ruth and Costa, 2021).

Regional implications for alkaline magmatism and Nb mineralization

The rock samples of the NV show high concentrations of both HFSE and LREE along with high Ce/Pb ratios (28–42) that infer the existence of garnet and amphibole phase via metasomatism in the HIMU-OIB mantle source, distinctive of within plate regime (Ball et al., 2019). The uniformity of isotope ratios characterizing the NV like $^{87}Sr/^{86}Sr$ = 0.7030–0.70286, $^{143}Nd/^{144}Nd$ = 0.512653–0.512761, $^{206}Pb/^{204}Pb$ = 19.28–19.94, and $^{177}Hf/^{176}Hf$ = 0.28274–0.28285 (Abu El Rus et al., 2018) reinforces metasomatized high μ HIMU-OIB mantle, similar to Late Proterozoic metasomatized mantle source in many volcanic fields like Mashriq and Bayuda, Sudan (Lotter et al., 2022) and Harrat, Saudi Arabia (Shaw et al. 2007). The metasomatic enhancement is primarily attributed to the emitting of subducted-related fluids/melts that have been proposed for the lithosphere mantle in the ANS during the Neoproterozoic Era (Stein et al. 1997; Abu El-Rus et al., 2018). The isotopic composition and geochemical features of NV along with alkaline ring complexes and Neogene volcanic fields worldwide have been inferred as the sign of the asthenospheric mantle source outpouring from mantle plume region (Fig. 14b, Hofmann, 2003; Niu et al., 2012) emphasizing the existence of high thermal instabilities (i.e. attendance of a deep mantle plume, Abu El Rus et al., 2018; Khalaf et al., 2018), similar to the St. Helena worldwide HIMU in the South Atlantic (Zhu et al., 2022).

The Nb-rich alkaline rocks chiefly extend in various tectonic settings involving craton borders, continental rifts, along with an extensional regime, and rare metal-rich deep source (Ballouard et al., 2020). Adiabatic decompression concomitant with crustal thinning triggers partial melting of the mantle via low degree to produce crucial alkaline melt in the continental rift setting (Khalaf et al., 2018). Temporarily, plate divergence with a low separation rate is encouraging to yield prevalent alkaline magmatism and

prompting provincial rare metal mineralization (Beard et al., 2022). Preceding investigations have revealed that the NE African Terrain (Egypt, Sudan, and Ethiopia) evolved from subduction during Neoproterozoic Era to wide-ranging extensional breakdown and continued until the Mid Neogene (Mohamed, 1998; Vail, 1989). The extensive alkaline magmatism recorded in the SED during the Late Cretaceous, Egyptian/Sudanese borders, Central Africa, Eastern Cameroon, and Kenya, along with Tanzania and Somalia coastal basins indicates that in the Natash area, SED was still in rift-related continental settings (Khalaf et al., 2018). The age resemblance between the NV and the other ring plutons in SED like El Kahfa ring complex (92 Ma, Serencsits et al., 1981; Lutz et al., 1988) infers a widespread alkaline magmatic episode in the Late Mesozoic Era. Regarding the chronological dispersion of alkaline rock assemblages in the SED, the outpouring of the asthenosphere triggered by the lithospheric breakdown protracted a highest during 94–86 Ma. A preferred model for formation of alkaline rocks and Nb-LREE enrichment in the SED is shown in Fig. 14c, as has been proposed for rare metal-rich alkaline rocks (Wu et al. 2023). During the Late Cretaceous, the regional extension of SED triggered the asthenosphere upwelling that is commonly transferred by an outpouring of volatile-rich melts transporting plentiful trace and rare earth elements (like HFSE and REE) from the deep mantle to the shallow lithospheric mantle (e.g. Huang et al., 2014; Yan et al., 2021, 2022). The latter was metasomatized by the continuous rise of such volatile-rich melts and fluids. Delamination and decompression melting into the convecting mantle facilitate the asthenospheric upwelling via diapiric mantle (Nixon et al. 2011). Crustal extension and lithospheric thinning prompted the partial melting of the metasomatic mantle during 96–86 Ma, forming alkaline OIB-like magmas enriched in Nb and REE. When the magmas ascend, fractional crystallization of olivine and pyroxene with exceedingly low $^{ol/liq}D_{Nb\text{-}REE}$ and $^{px/liq}D_{Nb\text{-}REE}$ subscribe the enhancement contents of incompatible rare metal elements (Foley et al., 2013; Beard et al., 2022). The greatly fractionated magmas ascend through the upper crust to create plutons or expelled to yield trachyandesitic/trachytic and rhyolitic extrusions. The HFSE-REE-bearing liquids rise and mingle with feldspar-rich rocks, resulting in the crucial formation of ore-forming elements.

Conclusion

Pervasive NW-SE trending alkaline rocks are well represented in Wadi Natash area with ages concentrating at 96 to 86 Ma. The Natash volcanoes display a wide compositional range, extending from basalts through trachyandesites and trachytes to rhyolites/comendites. The trachyandesites/trachytes and rhyolites of the NV show distinctive geochemical features like high HFSE and Ga/Al along with low ratio of Y/Nb and contents of Sr, P, Ti, and Eu, revealing A_1-type granite. The enrichment of both HFSEs and LREEs, analogous to the OIB-type rocks, shows that NV were produced by partial melting of a metasomatized lithospheric mantle triggered by asthenosphere-derived melts that lead to the Nb and REE-rich primary magma, followed by prolonged fractional crystallization with negligible role of the crustal contamination. Consequences of the geobarometric calculations reveal comprehensive storage zones ranging from the uppermost crust (~26–9 km depth) to deep mid crustal levels (~50–43 km depth), enlightening a crystal-rich magma mushes (dominant feldspar). The NV are enriched in Nb-REEs that were originally dominated by high degree of fractional crystallization and then imposed by the hydrothermal metasomatism. The Natash volcanoes are one of the well-known large-scale alkaline magmatic events generated in an extensional regime in the SED during the Late Mesozoic Era, inferring that the Rodinia assembly had been finalized prior to ca. 86 Ma.

Supplementary Information The online version contains supplementary material available at https://doi.org/10.1007/s12517-023-11637-1.

Acknowledgements We acknowledge Dr. Federico Lucci, Department of Earth and Geoenvironmental Sciences, University of Bari Aldo Moro, Italy, and Dr. Nils Lenhardt, Department of Geology, University of Pretoria, for reading the draft of this manuscript. A lot of thanks to Dr. Yukiyasu Tsutsumi who made geochronological work at the National Museum of Science, Japan. An anonymous reviewer improved the quality of the paper and is gratefully acknowledged.

Funding Funding of this research was partly provided by an invitational fellowship for research in Japan from the Japan Society for the Promotion of Science (JSPS S17025).

Declarations

Competing interests The authors declare no competing interests.

References

Abu El-Rus MA, Chazot G, Vannucci R, Gahlan HA, Boghdady GY, Paquette JL (2016) Softening of sub-continental lithosphere prior rifting: evidence from clinopyroxene chemistry in peridotite xenoliths from Natash volcanic province, SE Egypt. J Volcanol Geotherm Res 327:84–98

Abu El-Rus MA, Chazot G, Vannucci R, Paquette JL (2018) Tracing the HIMU component within Pan-African lithosphere beneath northeast Africa: evidence from Late Cretaceous Natash alkaline volcanoes, Egypt. Lithos 300(301):136–153

Abu El-Rus MA, Paquette JL, Chazot G, Vannucci R (2019) Bimodal zircon ages from Natash volcanics (southeast Egypt) and the link between eruption mechanisms and Late Cretaceous tectonics. Arab J Geosci 12:291. https://doi.org/10.1007/s12517-019-4457-2

Aiuppa A, Fischer T, Plank T, Bani P (2019) CO_2 flux emissions from the earth's most actively degassing volcanoes, 2005–2015. Sc Rep-UK 9:5442. https://doi.org/10.1038/s41598-019-41901-y

Ball PW, White NJ, Masoud A, Nixon S, Hoggard MJ, Maclennan J, Stuart FM, Oppenheimer C, Kropelin S (2019) Quantifying asthenospheric and lithosphericcontrols on mafic magmatism across North Africa. Geochem Geophys Geosyst 20(7):3520–3555

Ballouard C, Poujol M, Boulvais P, Branquet Y, Tartese R, Vigneresse JL (2016) Nb-Ta fractionation in peraluminous granites: a marker of the magmatic- hydrothermal transition. Geology 44:231–234

Ballouard C, Massuyeau M, Elburg MA, Tappe S, Viljoen F, Brandenburg JT (2020) The magmatic and magmatic-hydrothermal evolution of felsic igneous rocks as seen through Nb-Ta geochemical fractionation, with implications for the origins of rare-metal mineralizations. Earth Sci Rev 203:103115

Beard CD, Goodenough KM, Borst AM, Wall F, Siegfried PR, Deady EA, Pohl C, Hutchison W, Finch AA, Walter BF, Elliott HAL, Brauch K (2022) Alkaline-silicate REE-HFSE systems. Econ Geol econgeo 118(1):177–208

Brenna M, Croning SJ, Smith EM, Mass R, Sohn SY (2012) How small-volume basaltic magmatic systems develop: a case study from the Jeju Island volcanic field, Korea. J Petrol 53:985–1018

Chandler R, Spandler C (2020) The igneous petrogenesis and rare metal potential of the peralkaline volcanic complex of the southern Peak Range, Central Queensland, Australia. Lithos 358:105386

Chung SL, Liu DY, Ji JQ, Chu MF, Lee HY, Wen DJ, Lo CH, Lee TY, Qian Q, Zhang Q (2003) Adakites from continental collision zones: melting of thickened lower crust beneath southern Tibet. Geology 31:1021–1024

CONOCO (1987) Geological map of Egypt, NG36 SE Gebel Hamata sheet, scale 1:500000. The Egyptian General Petroleum Corporation, Cairo, Egypt

Coote A, Shane P (2018) Open-system magmatic behavior beneath monogenetic volcanoes revealed by the geochemistry, texture and thermobarometry of clinopyroxene, Kaikohe-Bay of Islands volcanic field (New Zealand). J Volcanol Geotherm Res 368:51–62

Crawford WA, Coulter DH, Hubbard HB (1984) The areal distribution, stratigraphy and major element chemistry of the Wadi Natash volcanic series, Eastern Desert, Egypt. J Afr Earth Sci 2:119–128

Cucciniello C, Le Roex AP, Jourdan F, Morra V, Grifa C, Franciosi L, Melluso L (2018) The mafic alkaline volcanism of SW Madagascar (Ankililoaka, Tulear region): 40Ar/39Ar ages, geochemistry and tectonic setting. Journal of the Geological Society 175:627–641. https://doi.org/10.1144/jgs2017-139

Danyushevsky LV, Plechov P (2011) Petrolog3: integrated software for modelling crystallization processes. Geochemistry, Geophysics, Geosystems 12:32. https://doi.org/10.1029/2011GC003516

Eby GN (1990) The A-type granitoids: a review of their occurrence and chemical characteristics and speculations on their petrogenesis. Lithos 26:115–134

Eby GN (1992) Chemical subdivision of the A-type granitoids: petrogenetic and tectonic implications. Geol 20:641–644

El-Shazly EM, Krs M (1973) Paleogeography and paleomagnetism of the Nubian sandstone, Eastern Desert of Egypt. Geol Rundsch 62:212–225

Eskandari A (2016) Evaluation of magmatic evolutions of damavand volcano based on the mineralogical and geochemical data. Kharazmi University (PhD thesis, in Persian)

Eskandari A, Amini S, De Rosa R, Donato P (2018) Nature of the magma storage system beneath the Damavand volcano (N. Iran): an integrated study. Lithos 300–301:154–176

Estrade G, Béziat D, Salvi S, Tiepolo M, Paquette JL, Rakotovao S (2014) Unusual evolution of silica-under- and -oversaturated alkaline rocks in the Cenozoic Ambohimirahavavy Complex (Madagascar): mineralogical and geochemical evidence. Lithos 206:361–383

Fan XZ, Sun FY, Xu H, Wu QQ, Yu L, Wang L, Yan C, Bakht S (2021) Volcanic rocks of the Elashan formation in the Dulan-Xiangride Basin, East Kunlun Orogenic Belt, NW China: petrogenesis and implications for Late Triassic geodynamic evolution. Int Geol Rev 64(9):1270–1293. https://doi.org/10.1080/00206814.2021.1923074

Firth CW, Handley HK, Cronin SJ, Turner SP (2014) The eruptive history and chemical stratigraphy of a post-caldera, steady-state volcano: Yasur, Vanuatu. Bull Volcanol 76:837. https://doi.org/10.1007/s00445-014-0837-3

Foley SF, Prelevic D, Rehfeldt T, Jacob DE (2013) Minor and trace elements in olivines as probes into early igneous and mantle melting processes. Earth Planet Sci Lett 363:181–191

Furman T, Graham D (1999) Erosion of lithospheric mantle beneath the East African Rift system: geochemical evidence from the Kivu volcanic province. Lithos 48:237–262

Garson MS, Krs M (1978) Geophysical and geological evidence of the relationship of Red Sea transverse tectonics to ancient fractures. Bull Geol Am 87:169–181

Girei MB, Li H, Algeo TJ, Bonin B, Ogunleye PO, Bute SI, Ahmed HA (2019) Petrogenesis of A-type granites associated with Sn–Nb–Zn mineralization in Ririwai complex, north-Central Nigeria: constraints from whole-rock Sm-Nd and zircon Lu-Hf isotope systematics. Lithos 340:49–70

Green DH, Falloon TJ (1998) Pyrolite: A ringwood concept and its current expression. In: Jackson I (ed) The earth's mantle: composition, structure, and evolution. Cambridge University Press, Cambridge, pp 311–378

Green DH, Falloon TJ (2005) Primarymagmas atmid-ocean ridges, 'hotspots', and other intraplate setting: constraints on mantle potential temperature. In: Foulger GR, Natland JH, Presnall DC, Anderson DL (eds), Plates, plumes, and paradigms. Geol Soci Amer, Spec Pap 388:217–247

Hashad MH (1994) Geochemical characteristics and petrogenesis of phonolite-trachyte plugs associated with Wadi Natash volcanic rocks. Middle East Research Center Ain Shams University Earth Sci Ser 8:131–145

Hashad AH, El-Reedy MWM (1979) Geochronology of the anorogenic alkalic rocks, south Eastern Desert. Egypt Ann Geol Surv Egypt 9:81–101

Hastie AR, Fitton JG, Mitchell SF, Neill I, Nowell GM, Millar IL (2015) Can fractional crystallization, mixing and assimilation processes be responsible for Jamaican-type adakites? Implications for generating Eoarchaean continental crust. J Petrol 56:1251–1284

Hastie AR, Mitchell SF, Kerr AC, Minifie MJ, Millar IL (2011) Geochemistry of rare high-Nb basalt lavas: are they derived from a mantle wedge metasomatised by slab melts? Geochim Cosmochim Acta 75:5049–5072

Harris C, Dreyer T, le Roux P (2018) Petrogenesis of peralkaline granite dykes of the Straumsvola complex, western Dronning Maud Land. Antarctica Contrib Mineral Petrol 173:8

Hegazy HA, Arzamastsev AA, Saad E (2016) Geology, petrography and geochemistry of El-kahfa ring complex, South Eastern Desert, Egypt. Inter J Geophys Geochem 3(3):25–37. https://www.researchgate.net/publication/310616757

Hofmann AW (2003) Sampling mantle heterogeneity through oceanic basalts: isotopes and trace elements. Treatise on Geochem 2:568

Holness MB, Stock MJ, Geist D (2019) Magma chambers versus mush zones: constraining the architecture of sub-volcanic plumbing systems from microstructural analysis of crystalline enclaves. Philos T R Soc S-A 377:20180006. https://doi.org/10.1098/rsta.2018.0006

Huang H, Zhang ZC, Santosh M, Zhang DY (2014) Geochronology, geochemistry and metallogenic implications of the Boziguo'er rare metal-bearing peralkaline granitic intrusion in South Tianshan, NW China. Ore Geol Rev 61:157–174

Khalaf EA, Sano T, Tsutsumi Y (2018) Evolution of monogenetic rift-related alkaline magmatism in south Egypt: insight from stratigraphy, geochronology, and geochemistry of the Natash volcanics. J Afr Earth Sci 147:450–476

Kelley KA, Cottrell E (2009) Water and the oxidation state of subduction zone magmas. Science 325:605–607

King PL, White AJR, Chappell BW, Allen CM (1997) Characterization and origin of aluminous A type granites from the Lachland fold belt, southeastern Australian. J Petrol 38:371–391

Kinzler RJ (1997) Melting of mantle peridotite at pressures approaching the spinel to garnet transition: application to mid-ocean ridge basalt petrogenesis. J of Geophys Res. https://doi.org/10.1029/96JB00988

La Flèche MR, Camiré G, Jenner GA (1998) Geochemistry of post-Acadian, Carboniferous continental intraplate basalts from the Maritimes Basin, Magdalen Islands, Québec. Canada Chem Geol 148(3–4):115–136

Landoll JD, Foland KA, Henderson CMB (1994) Nd isotopes demonstrate the role of contamination in the formation of coexisting quartz and nepheline syenites at the Abu Khruq complex. Egypt Contrib Mineral Petrol 117:305–329

Li XK, Chen J, Wang RC, Li C, Wang M, Liu JH, Yu YP, Luo AB (2019) Early Cretaceous tectonomagmatic evolution and basin development of western Bangong-Nujiang suture: a complete history of soft collision. Lithos 344–345:360–373

Lotter FJP, Lenhardt N, Viereck L, Münker C, Marien CS, Altigani MAH (2022) The Quaternary monogenetic Bayuda Volcanic Field, Sudan – insights into mantle and crustal processes during magma petrogenesis. Lithos 410–411:106563

Lutz TM et al (1988) The strontium and oxygen isotopic record of hydrothermal alteration of syenites from the Abu Khruq complex, Egypt. Contrib Mineral Petrol 98:212–223

Martin R (2006) A-type granites of crustal origin ultimately result from open-system fenitization-type reactions in an extensional environment. Lithos 91:125–136

Marzoli A, Aka FT, Merle R, Callegaro S, Nni J (2015) Deep to shallow crustal differentiation of within-plate alkaline magmatism at Mt. Bambouto volcano, Cameroon Line. Lithos 220–223:272–288

McCarthy A, Chelle-Michou C, Blundy JD, Vonlanthen P, Meibom A, Escrig S (2020) Taking the pulse of volcanic eruptions using plagioclase glomerocrysts. Earth Planet Sci Lett 552:116596

McCoy-West AJ, Baker JA, Faure K, Wysoczanski R (2010) Petrogenesis and origins of mid-cretaceous continental intraplate volcanism in Marlborough, New Zealand: implications for the long-lived HIMU magmatic Mega-province of the SW Pacific. J Petrol 51:2003–2045

McKenzie D, O'Nions RK (1995) Partial melt distributions from inversion of rare Earth element concentrations. J Petrol 32:1021–1091

Meneisy MY (1986) Mesozoic igneous activity in Egypt. Qatar Univ Sci Bull 6:57–72

Miller RR (2015) Pantellerite-hosted rare earth element mineralization in Southeast Labrador: the Foxtrot deposit. In: Simandl GJ, Neetz M (eds) Symposium on Strategic and Critical Materials Proceedings, vol 2015-3. British Columbia Geological Survey Paper, pp 109–117

Miller CF, McDowell SM, Mapes RW (2003) Hot and cold granites? Implications of zircon saturation temperatures and preservation of inheritance. Geol 31:529–532

Mohamed FH (1998) Geochemistry and petrogenesis of El Gezira ring complex, Egypt: a monzosyenite cumulate derived from fractional crystallization of trachyandesitic magma. J Volcanol Geotherm Res 84:103–123

Mogahed MM (2016) Petrogenesis of cogenetic silica-oversaturated and -undersaturated syenites of Abu Khruq ring complex, South Eastern Desert, Egypt. J Afr Earth Sci 124:44–62. https://doi.org/10.1016/j.jafrearsci.2016.09.010

Münker C, Pfänder JA, Weyer S, Büchl A, Kleine T, Mezger K (2003) Evolution of planetary cores and the Earth-Moon system from Nb/Ta systematics. Science 301:84–87

Murcia H, Borrero C, Németh K (2019) Overview and plumbing system implications of monogenetic volcanism in the northernmost Andes' volcanic province. J Volcanol Geotherm Res 383:77–87

Németh K (2010) Monogenetic volcanic fields: origin, sedimentary record, and relationship with polygenetic volcanism. In: Cañón-Tapia E, Szakács A (eds) What is a volcano? Special Papers, vol 470. Geological Society of America, Boulder, Colorado, pp 43–67

Nimis P (1999) Clinopyroxene geobarometry of magmatic rocks. Part 2. Structural geobarometers for basic to acid, tholeiitic and mildly alkaline magmatic systems. Contrib Mineral and Petrol 135:62–74

Niu YL, Batiza R (1997) Trace element evidence from seamounts for recycled oceanic crust in the eastern pacific mantle. Earth Planet Sci Lett 148:471–483

Niu Y, O'Hara MJ (2003) Origin of ocean island basalts: a new perspective from petrology, geochemistry, and mineral physics considerations. J Geophys Res 108:B4

Niu Y, Wilson M, Humphreys ER, O'Hara MJ (2011) The origin of intra-plate ocean island basalts (OIB): the lid effect and its geodynamic implications. J Petrol 52:1443–1468

Niu Y, Wilson M, Humphreys ER, O'Hara MJ (2012) A trace element perspective on the source of ocean island basalts (OIB) and fate of subducted ocean crust (SOC) and mantle lithosphere (SML). Episodes 35(2):310–327

Nixon S, Maclennan J, White N (2011) Intra-plate magmatism of the Al Haruj Volcanic Field, Libya. In: Goldschmidt conference abstracts

Omar GI, Kohn BP, Lutz TM, Faul H (1987) The cooling history of Silurian to cretaceous alkaline ring complexes, south Eastern Desert, Egypt, as revealed by fission-track analysis. Earth Planet Sci Lett 83:94–108

O'Neill HSC (1981) The transition between spine1 lherzolite and garnet lherzolite, and its use as a geobarometer. Contrib Mineral Petrol 77:185–194

Paces JB, Miller JD (1993) Precise U-Pb ages of Duluth Complex and related mafic intrusions, northeastern Minnesota: geochronological insights to physical, petrogenetic, paleomagnetic, and tectonomagmatic processes associated with the 1.1 Ga midcontinent rift system. J Geophys Res 98:13997–14013

Pearce JA (2008) Geochemical fingerprinting of oceanic basalts with applications to ophiolite classification and the search for Archean oceanic crust. Lithos 100:14–48

Pilet S, Baker MB, Stolper EM (2008) Metasomatized lithosphere and the origin of alkaline lavas. Science 320:916–919

Pilet S, Baker MB, Münterner O, Stolper EM (2011) Monte Carlo simulations of metasomatic enrichment in the lithosphere and implications for the source of alkaline basalts. J Petrol 52(7–8):1415–1442

Pfänder JA, Münker C, Stracke A, Mezger K (2007) Nb/Ta and Zr/Hf in ocean island basalts—implications for crust–mantle differentiation and the fate of niobium. Earth Planet Sci Lett 254:158–172

Pontesilli A, Brenna M, Mollo S, Masotta M, Nazzari M, Le Rouxe P, Scarlato P (2022) Trachyte-phonolite transition at Dunedin Volcano: fingerprints of magma plumbing system maturity and mush evolution. Lithos 408–409(2022):106545

Putirka KD (2008) Thermometers and barometers for volcanic systems. Rev Mineral Geochem 69:61–120

Raghuvanshi S, Pandey A, Pankaj P, Rao NVC, Chakrabarti R, Pandit D, Pandey R, Hari KR (2019) Lithosphere-asthenosphere interaction and carbonatite metasomatism in the genesis of mesoproterozoic shoshonitic lamprophyres at Korakkodu, Wajrakarur kimberlite field, Eastern Dharwar Craton, southern India. Geol J 54:3060–3077

Renjith ML (2014) Micro-textures in plagioclase from 1994–1995 eruption, Barren Island Volcano: evidence of dynamic magma plumbing system in the Andaman subduction zone. Geosci Front 5:113–126

Roeder PL, Emslie RF (1970) Olivine-liquid equilibrium. Contrib Mineral Petrol 29:275–289

Rooney TO, Nelson WR, Dosso L, Furman T, Hanan B (2014) The role of continental lithosphere metasomes in the production of HIMU-like magmatism on the northeast African and Arabian plates. Geol 42(5):419–422

Rudnick RL, Gao S (2003) In: Rudnick RL (ed) The composition of the continental crust. The crust, pp 1–64

Ruth DSC, Costa F (2021) A petrological and conceptual model of Mayon Volcano (Philippines) as an example of an open-vent volcano. Bull Volcanol 83:62. https://doi.org/10.1007/s00445-021-01486-9

Sahoo S, Chalapathi Rao NV, Monié P, Belyatsky B, Dhote P, Lehmann B (2020) Petrogeochemistry, Sr-Nd isotopes and 40Ar/39Ar ages of fractionated alkaline lamprophyres from the Mount Girnar igneous complex (NW India): insights into the timing ofmagmatismand the lithosphericmantle beneath the Deccan large igneous province. Lithos. https://doi.org/10.1016/j.lithos.2020.105712

Saleh GM, Mira H, Kamar MS (2021) Phanerozoic minor volcanics and intrusives of the Arabian-Nubian shield. The Geology of the Arabian-Nubian Shield, Regional Geology Reviews. https://doi.org/10.1007/978-3-030-72995-0_26

Salters VJM, Stracke A (2004) Composition of the depleted mantle. Geochem Geophys Geosyst 5:Q05B07. https://doi.org/10.1029/2003GC000597

Sajona FG, Maury RC, Bellon H, Cotton J, Defant MJ (1996) High field strength element enrichment of Pliocene–Pleistocene island arc basalts, Zamboanga Peninsula, Western Mindanao (Philippines). J Petrol 37:693–726

Sano T, Shirao M, Tani K, Tsutsumi Y, Kiyokawa S, Fujii T (2016) Progressive enrichment of arc magmas caused by the subduction of seamounts under Nishinoshima volcano, Izu-Bonin Arc, Japan. J Volcanol Geoth Res 319:52–65

Shao FL, Niu YL, Regelous M, Zhu DC (2015) Petrogenesis of peralkaline rhyolites in an intra-plate setting: Glass House Mountains, southeast Queensland, Australia. Lithos 216:196–210

Shaw DM (1970) Trace element fractionation during anatexis. Geochim Cosnochim Acta 34(237–37):259

Shaw JE, Baker JA, Kent JR, Ibrahim KM, Menzies MA (2007) The geochemistry of the Arabian lithospheric mantle—a source for intraplate volcanism? J Petrol 48:1495–1512

Sheard ER, Williams-Jones AE, Heiligmann M, Pederson C, Trueman DL (2012) Controls on the concentration of zirconium, niobium, and the rare earth elements in the Thor Lake rare metal deposit, Northwest Territories. Canadan Econ Geol 107:81–104

Sen G, Chandrasekharan D (2011) Deccan traps flood basalt province, An evaluation of the thermochemical plume model. In: Ray J, Sen G, Ghosh B (eds) Topics in igneous petrology. Springer, Dordrecht

Serencsits CM et al (1981) Alkaline ring complexes in Egypt: their ages and relationship in time. J Geophys Res Solid Earth 86:3009–3013

Spath A, Le Roex AP, Opiyo-Akech N (2001) Plume–lithosphere interaction and the origin of continental rift-related alkaline volcanism—the Chyulu Hills volcanic province, Southern Kenya. J Petrol 42(4):765–787

Stacey G, Kramers M (1975) UKinrek maars, Alaska, II Deposits and crater formation. J Volcanol Geothermal Res 7:39–65

Stein M, Navon O, Kessel R (1997) Chromatographic metasomatism of the Arabian Nubian lithosphere. Earth Planet Sci Lett 152:75–91

Stepanov A, Mavrogenes JA, Meffre S, Davidson P (2014) The key role of mica during igneous concentration of tantalum. Contrib Mineral Petrol 167:1009–1016

Sun SS, McDonough WF (1989) Chemical and isotopic systematics of oceanic basalts: implications for mantle composition and processes. In: Saunders AD, Norry MJ (eds) Magmatism in the ocean basins, vol 42. Geol Soci Lond Spec Publ, pp 313–345

Taylor SR, McLennan SM (1985) The continental crust: its composition and evolution. Blackwell Scientific Publication, Oxford

Timofeev A, Migdisov AA, Williams-Jones AE (2015) An experimental study of the solubility and speciation of niobium in fluoride-bearing aqueous solutions at elevated temperature. Geochim Cosmochim Acta 158:103–111

Tsutsumi Y, Horie K, Sano TT, Mijawaki K, Momma S, Sigeoka M, Yokoyama K (2012) LA-ICP-MS and SHRIMP ages of zircons in Chevkinite and monazite tuffs from the Boso Peninsula. Central Japan Bull Nat Mus Nat Sci Tokyo C38:15–32

Vail JR (1989) Ring complexes and related rocks in Africa. J Afr Earth Sci 8:19–40

Wang Q, Wyman DA, Xu J, Jian P, Zhao Z, Li C, Xu W, Ma J, He B (2009) Early Cretaceous adakitic granites in the Northern Dabie complex, Central China: implications for partial melting and delamination of thickened lower crust. Geochim Cosmochim Acta 71(10):2609–2636

Wang K, Wang LX, Ma CQ, Zhu YX, She ZB, Deng X, Chen Q (2021) Mineralogy and geochemistry of the Zhuxi Nb-rich trachytic rocks, South Qinling (China): insights into the niobium mineralization during magmatic-hydrothermal processes. Ore Geol Rev 138:104346

Weinstein Y, Navon O, Altherr R, Stein M (2006) The role of lithospheric mantle heterogeneity in the generation of Plio-Pleistocene alkali basaltic suites from NWHarrat Ash Shaam (Israel). J Petrol 47:1017–1050

Winchester JA, Floyd PA (1976) Geochemical magma type discrimination: application to altered and metamorphosed basic igneous rocks. Earth Planet Sci Lett 28:459–469

Weaver BL (1991) The origin of ocean island basalts end-member composition: trace element and isotopic constraints. Earth Planet Sci Lett 104:381–397

Weng ZH, Jowitt SM, Mudd GM, Haque N (2015) A detailed assessment of global rare earth element resources: opportunities and challenge. Econ Geol 110(8):1925–1952

Willbold M, Stracke A (2006) Trace element composition of mantle end-members: implications for recycling of oceanic and upper and lower continental crust. Geochem Geophys Geosyst 7. https://doi.org/10.1029/2005GC001005

Whalen JB, Currie KL, Chappell BW (1987) A-type granites: geochemical characteristics, discrimination and petrogenesis. Contrib Mineral Petrol 95:407–419

Wood BJ (2004) Melting of fertile peridotite with variable amounts of H2O. Geophys Monogr 150:69–80

Wu H, Huang H, Zhang Z, Wang T, Guo L, Gao Y, Zhang Z (2023) Highly differentiated trachytic magma linked with rare metal mineralization: a case study from the Shuanghekou Nb deposit, South Qinling. Lithos 438–439:106990

Xiang YX, Yang JH, Chen JH, Zhang Y (2017) Petrogenesis of Lingshan highly fractionated granites in the Southeast China: implication for Nb-Ta mineralization. Ore Geol Rev 89:495–525

Xu HJ, Zhang JF, Wang YF, Liu WL (2016) Late Triassic alkaline complex in the Sulu UHP terrane: implications for post-collisional magmatism and subsequent fractional crystallization. Gondwana Res 35:390–410

Yan S, Shan Q, Niu HC, Yu X, Zhao X, Zhang HJ, Xiong Y (2021) Timing and genesis of the Tudiling trachyte Nb-Ta-Zr-REE deposit in the South Qinling (Central China): implications for rare metal enrichment in extrusive peralkaline magmatic systems. Ore Geol Rev 139:104535

Yan S, Niu HC, Zhao X, Zhang QB, Zhang HJ, Zhao XC (2022) Rare metal enrichment of the Tianbao trachytic complex, North Daba Mountains (South Qinling): insights from textures and geochemistry of trachytes and Nb-REE minerals. Ore Geol Rev 146:104948

Yang JH, Wu FY, Chung SL, Wilde SA, Chu MF (2006) A hybrid origin for the Qianshan A-type granite, Northeast China: geochemical and Sr–Nd–Hf isotopic evidence. Lithos 89:89–106

Zhang FY, Lai SC, Qin JF, Zhu RZ , Zhao SW, Zhu Y, Yang H (2020) Vein- plus-wall rock melting model for the origin of early Paleozoic alkali diabases in the South Qinling Belt, Central China. Lithos 370–371

Zhu YS, Yang JH, Sun JF, Zhang JH, Wu FY (2016) Petrogenesis of coeval silica saturated and silica-undersaturated alkaline rocks: mineralogical and geochemical evidence from the Saima alkaline complex, NE China. J Asian Earth Sci 117:184–207

Zhu YX, Wang LX, Xiong QH, Ma CQ, Zhang X, Zhang C, Ahmed HA (2020) Origin and evolution of ultrapotassic intermediate magma: the Songxian syenite massif, Central China. Lithos 366–367:105554

Zhu H, Hoernle K, Geldmacher J, Hauff F, Hormrighausen S, Garbesconberg S, Binderman I (2022) A HIMU volcanic belt along the SW African coast (~83–49 Ma): new geochemical clues to deep mantle dynamics from carbonatite and silica-undersaturated complexes in Namibia. Lithos 430-431:106839